The effect of diffusion on P-T conditions inferred by cation-exchange thermobarometry

Alexandra Andrews
Advisor: Dr. Zhengrong Wang
Second Reader: Dr. Edward Bolton
April 27, 2011

A Senior Thesis presented to the faculty of the Department of Geology and Geophysics, Yale University, in partial fulfillment of the Bachelor's Degree.

Abstract

Mantle xenoliths are used to infer geothermal gradients of the sub-continental lithospheric mantle through cation exchange thermobarometry. This method assumes that cations reach thermodynamic equilibrium at depth and maintain this state during their ascent to the Earth's surface. We examined a suite of garnet peridotites from the Kaapvaal craton (Kimberley, South Africa). Rock sections containing garnet, cpx, opx, and olivine were mounted and measured for their major element compositions at Yale University using the JEOL JXA-8530F field emission gun electron microprobe. P-T conditions calculated for these samples using BKN thermobarometry vary from 930–1240°C and 39–52 kbar. More interestingly, chemical zoning is evident in garnet grains with radii varying from 400–1550 μm. This zoning produces P-T differences of 22–144°C and 1.5–6.3 kbar between rims and cores.

Analyses of these results suggest that the equilibrium assumption is not always valid due to diffusion and re-equilibration. Our observations include: 1) element diffusion profiles in minerals; 2) different P-T conditions inferred from rims and cores of coexisting minerals (particularly hotter and deeper P-T conditions calculated for the rims of some mineral assemblages than P-T calculations for the cores); 3) more scattered P-T conditions at higher pressures and temperatures. Calculations using Dodson's model for closure temperature show that zoning in xenoliths affects the definition of the curvature of the geotherm and consequently the parameter for the heat flux from the mantle.

Using these calculations, the discrepancy from Rudnick and Nyblade's geotherm is most apparent at depth.

The framework for a multi-component diffusion model was formulated for $Ca^{2+}/Mg^{2+}/Fe^{2+}$ exchange across garnet, cpx, opx, and olivine assemblages. Modeling results are pending but will be checked against the observed diffusion profiles. The Dodson calculations suggest that P-T conditions recorded in these mantle minerals depend on the cooling rate, crystal grain size, and geothermal gradient, which might not be the same as the linear regressed line through all calculated P-T conditions. This observation will be rigorously tested using the quantitative results of the pending diffusion model.

Introduction

Geothermal gradients (geotherms) are curve fit profiles based on measured and estimated physical parameters, including the concentration of radionuclides, the thickness of the lithospheric mantle, thermodiffusivity, and the heat flux from the asthenosphere. The resulting profile predicts how temperature varies with depth (pressure) in the lithosphere of a planetary body. In the Earth, radiogenic heat production and secular cooling are the most significant parameters in determining geotherms (Spear, 1993). Radioactive isotopes with long half-lives (^{235}U, ^{238}U, ^{232}Th, and ^{40}K) are a major source of thermal energy in the crust because the kinetic energy of alpha (α) particles, beta (β) particles, and γ-rays released during radioactive decay is converted to heat. The second significant parameter for fitting geotherms is the heat flux created by the cooling of the planet's interior (Spear, 1993). This heat flux (secular cooling) decreases with the age of

the planet but remains an important heat source for Earth's present and past geothermal calculations.

Understanding how the Earth's geothermal gradient has changed throughout history has important implications for many of Earth's processes. The surface geotherm and the heat flux of the current continental lithosphere can be directly measured in boreholes up to a little more than 12 km depth, but evidence for ancient temperature profiles of the subcontinental lithosphere is inferred only using mantle peridotite geothermobarometry (Boyd, 1973). With techniques pioneered by Boyd, temperatures and pressures of equilibration in the lithospheric mantle can be determined for mantle peridotites (O'Neill and Wood, 1979; Nickel and Green, 1985, Carswell and Gibb, 1987; Krogh, 1988; Brey and Kohler, 1990; Kohler and Brey, 1990, Nimis and Taylor, 2000). Generating geotherms is important because knowledge of the Earth's thermal history furthers our understanding of the structure and evolution of the mantle (Boyd, 1973). Mantle structure has been a controversial topic in the solid Earth sciences since the late 1970's and remains so today (Korenaga, 2008). As mantle xenoliths are the only direct samples from the mantle, the data and information derived from geothermobarometry provide crucial constraints on delineations of mantle structure and convection. These constraints contribute to forming an increasingly precise model of mantle convection. Such models have a profound impact on areas of Earth science from studies of plate tectonics and continental growth to the evolution of life and the surface environment (Tackley, 2000; Bercovici, 2003; Hager and O'Connell, 1981; Bercovici et. al., 2000; Tackley, 1998; Rudnick and Nyblade, 1999; Gurnis, 1988; Santosh, 2010).

Mantle xenoliths are used in geothermobarometry to calculate the pressures and temperatures of the lithospheric mantle. By recording cation exchange between minerals in xenolith assemblages, geothermobarometers have been developed to deduce the temperatures and pressures at which samples equilibrated. These models typically make the following key assumptions. First, many mantle xenolith samples exhibit little or no zoning (Rudnick and Nyblade, 1999). Given calculations of kimberlite magma ascent and lack of evidence for element zoning within the minerals, it is widely believed that mantle xenoliths do not re-equilibrate at shallower depths and lower temperatures during ascent (McGetchin, 1968; McGetchin and Ullrich, 1973; Smyth and Hatton, 1977; O'Hara et. al., 1971; Mercier, 1979; McCallister et. al. 1979; Ganguly, 1981; Mitchell, 1979; Canil and Fedortchouck, 1999; Rutherford and Gardener, 2000; Basson and Viola, 2004; Wilson and Head, 2007). If re-equilibration occurs during ascent to the surface, then the pressure and temperature estimates obtained from thermobarometers would be lower than the pressures and temperatures of original equilibration and this assumption would not be valid.

Despite the vast literature supporting the idea that xenoliths record the deepest and hottest equilibration conditions, zonation in xenoliths has been recorded by Smith and Boyd (1992), Kopylova et. al. (1999), and Pre et. al. (1986), among others. Given samples that exhibit zoning, the assumption of chemical equilibration at original depths of formation does not hold true. The presence of zoning suggests additional or alternative processes occurring at the sites producing these assemblages. For these zoned samples, kinetics may play a significant role in determining the pressure-temperature data. This study investigates the importance of diffusion for geothermobarometric

calculations of zoned samples. If diffusion causes vast variations in P-T calculations, then the assumption of equilibration at depth may become uncertain for un-zoned samples as well.

The second assumption of geothermobarometry is the level of geothermobarometer precision. These models produce a wide range of pressures and temperatures for xenoliths from the same pipes and vastly different pressures and temperatures for samples from different cratons (Finnerty and Boyd, 1984; Rudnick and Nyblade, 1999). The inconsistency of the results shows that there may be significant errors in the pressure-temperature data obtained.

The third assumption is craton stability. It is assumed that xenoliths erupt through cratons—geologically inactive, stable regions of the continental crust with low homogenous surface heat flux (Morgan 1984; Nyblade and Pollack, 1993). Cratons are parts of continents that have been tectonically inactive for billions of years; they are the remnants of ancient continents that comprise the core of continents today (Stille, 1936; Hoffman, 1988; Hoffman, 1989). Underneath cratons, there are large volumes of mantle that are convectively isolated from the asthenosphere over billion year timescales (Richardson et. al., 1984; Walker et. al., 1989; Pearson et. al., 1995a; Carlson et. al. 1999; Lee, 2006). This isolated mantle material provides a reservoir from which mantle samples of Archean origin can ascend to the surface. Thus, when eruption occurs in kimberlite pipes, the entrained samples are of Archean origin and do not represent mantle processes and conditions at the time of eruption.

In order to ensure that the samples are derived from Archean mantle material, as the geothermobarometric calculations assume, craton stability must be established.

Despite these three significant assumptions and the resulting limitations of the pressure and temperature data produced from geothermobarometers, thermobarometric calculations are the only direct data we have for the temperatures and pressures of the mantle.

Geothermal gradients and the temperatures and pressures of geothermobarometric studies are inextricably linked. Geotherms are not first principle equations; they are curve-fit profiles that are dependent on the input parameters and the values that are used for these variables. Even though they are curve-fit profiles, geotherms are valuable inferences for modeling temperature variation at depth. Since mantle xenolith data gives information about these temperatures and pressures, the relationship between these two plots is significant.

In the existing literature, there are three proposed models that relate geotherms with mantle xenolith data. Rudnick and Nyblade (1999) generated 18,000 geotherms using various input parameters to find a best-fit geotherm given a compilation of data from the Kalahari craton. Their model uses linear and second-order least squares regressions to determine 95% confidence limits of the pressure and temperature data. Then, they use a range of input parameters to find a geotherm that is most similar to a best-fit line for the data. Rudnick and Nyblade define their most successful geotherm as the profile with the lowest RMS error compared to the regressed pressure-temperature data (Rudnick and Nyblade, 1999). This model is the most accepted relationship between xenolith data and the geotherm. However, given the assumptions of geothermobarometric modeling, the pressures and temperatures obtained may not be an accurate representation

of the equilibration conditions. This error would be reproduced in Rudnick and Nyblade's geotherm as it is dependent on the array of pressure-temperature data points.

The second model in the literature was proposed by Pollack and Chapman in 1977. This model is based on surface heat flow and was constructed using Sclater and Francheteau's 1970 model of heat production in the crust and upper mantle. Sclater and Francheteau define the base of the crust as the boundary between a depleted ultrabasic zone (heat production of 10^{-2} μW m^{-3}) and an underlying pyrolite layer (heat production of 0.084 μW m^{-3}). Pollack and Chapman's geotherm is dependent on the 0.084 μW m^{-3} heat production value of the lithospheric mantle because the lithospheric mantle pyrolite layer is the significant contributor to surface heat flux (Pollack and Chapman, 1977). Since 1970, the accepted values for the heat production of the lithospheric mantle have dropped to a range of 0-0.07 μW m^{-3}, with many models suggesting values on the middle to lower end of this range, such as the 0.03 μW m^{-3} estimate of Michaut et. al. (2007). Since the curvature of the geotherms produced is dependent on the value of heat production in the lithospheric mantle and these values have changed since Pollack and Chapman's calculations, Pollack and Chapman's geotherm is not a good indicator of how the temperature profile is varying at depth.

Xenolith suites containing the necessary coexisting phases for geothermobarometry are rare. Therefore, Ryan and Griffin (1996) have proposed a thermobarometer and associated geotherms for individual garnet grains as remnants of disaggregated xenoliths in heavy-mineral concentrates (Ryan and Griffin, 1996). These methods are in sharp contrast to the other geothermobarometers and geotherms in the literature that are based on xenolith mineral assemblages, not solely based on one

mineral. The barometer used (P_{Cr}) depends on chromium (Cr) saturation during garnet formation in the mantle (this implies garnet-chromite co-existence). At temperatures below 1100°C, the samples that were formed in a Cr-saturated environment would yield reasonable pressures. However, the samples that grew without the presence of chromite would produce underestimates of true pressures because of errors in the barometer given by its dependence on Cr solubility. According to Ryan and Griffin, chromite is rare in cratonic mantle rocks at temperatures greater than 1100°C. Thus, the temperatures and pressures produced at higher temperatures are no longer valid, and the resulting geotherm is not defined in a meaningful way.

The geotherms determined for temperatures below 1100°C may also contain high errors based on the assumptions used. The original assemblages are unknown, so it is impossible for the authors to decipher the samples that equilibrated in the presence of chromite from the samples that did not. Thus, the garnet geotherms determined by visual inspection cannot take only the most accurate data into account but must take all the data produced into account. Geotherms produced under these conditions are not mathematically rigorous. In addition, the geotherms produced in Griffin's more recent papers (Griffin et. al., 2003) are compared to the geotherm defined by Pollack and Chapman (1977). As described above, Pollack and Chapman's geotherm was determined based on the estimates of lithospheric mantle heat production of the late 1970s, resulting in a geotherm with a flawed curvature, particularly at depth. Because Ryan and Griffin (1996) compare their geotherm and pressure-temperature results to this erroneous geotherm, the confirmation they receive is invalid.

The studies mentioned above have been conducted under the premise that mantle xenoliths preserve temperatures and pressures of equilibrium conditions at depth. However, it has been shown (Kopylova et. al.,1999; Pre et. al., 1986) that some xenolith samples are zoned. In the case that xenolith samples are zoned, equilibrium conditions have not been achieved and kinetics become relevant in thermobarometric calculations. This study investigates the role of kinetics and diffusion on temperatures and pressures of thermobarometric calculations and the affect these corrections will have on the geotherm.

Samples

The samples used in this project are mantle nodules from the Bultfontein Floors in Kimberley, South Africa; they were collected in March of 1977. During the early mining days, the material from several kimberlite pipes (e.g. Bultfontein, De Beers, and Wesselton) was placed in the area of the Bultfontein Floors to weather. Weathering softened the kimberlite material and made processing much easier. Thus, the kimberlite at the Bultfontein Floors altered and became friable, leaving the unaffected mantle nodules. The specific pipe origins of these nodules is unknown, but they were collected from the Floors and sent to Yale's Dept. of Geology and Geophysics, Jill Pasteris at the Dept. of Earth and Planetary Sciences at Washington University in Saint Louis, and the De Beers Geology Dept. Marie Schneider (Yale '79) did her senior project on the petrology of these samples (Pasteris, 1979).

Methods

Electron Microprobe

Mineral compositions from seven xenolith samples and thirty-three assemblages were determined using Yale University's Jeol JXA-8530F Field Emission Electron Probe Microanalyzer (EPMA). The analyses were made with an accelerating voltage of 15 kV and beam currents of 5 to 20 nA. The beam diameter varies from 0 to 10 microns, and the measurements were made using wavelength-dispersive spectrometry (WDS-only) and previously established standards. ZAF correction was used.

Core and rim compositions were measured for garnet and the surrounding minerals of thirty three garnet assemblages. Some of the surrounding phases include olivine, orthopyroxene, clinopyroxene, chromite, phlogopite, serpentine, amphibole, and chlorite. This data is reported in Tables 1-8 of the appendix.

Transects were also measured across three garnet assemblages—BU 6, BU 21, and BU 29. The BU 6 transect measures chemical compositions at 5E-5 meter increments from the garnet's core to rim over a distance of 4.5E-4 meters. The second half of the transect measures the clinopyroxene grain adjacent to the garnet at 5E-5 meter increments for 9.5E-4 meters from rim to core. An image of BU 6 transect locations is included in the appendix under images, and the composition data is included as Table 9. The BU 21 transect measures an olivine grain adjacent to the garnet on the left, the garnet in the center of the assemblage, and a clinopyroxene grain to the right of the garnet. Chemical compositions of the olivine and clinopyroxene segments were taken at 5E-5 meter intervals. Inside the garnet, four segments were made. The two segments closest to the rims (one on the left and one on the right) were measured at 5E-5 meter

increments, and the two segments in the core of the mineral were measured at 1E-4 meter spacing. The transect distances for olivine and orthopyroxene are 8E-4 meters. From left to right, the four garnet traverse segments cover distances of 8E-4 meters, 7E-4 meters, 1.2E-3 meters, and 6E-4 meters, respectively. A traverse image of the BU 21 transect is included in the appendix under images, and data is attached in Table 10. The BU 29 traverse crosses three mineral grains: olivine, garnet, and a second olivine. The segments in the olivine grains measure compositions every 5E-5 meters. The traverse across the olivine (located above the garnet) measures 8E-4 meters from core to rim, and the olivine below the garnet measures 5.5E-4 meters. Inside the garnet, there are three sections. The two fragments adjacent to the rim are recorded at 5E-5 meter intervals. The middle segment is measured every 1E-4 meters. Each of the three sections that span the rim-core-rim segments in the garnet is 6E-4 meters. An image of the BU 29 transect is included in the appendix under images, and data is included in Table 11.

Geothermobarometry

Over the last forty years, many thermometers and barometers have been created by tracing various cation exchanges across particular mineral assemblages. Five combinations of these thermometers and barometers were compiled in this study to procure the most accurate temperatures and pressures, as compared to experimental results in the literature. Because some thermometers and barometers make better estimates than others under specific conditions, this study used a variety of models to maximize accuracy. The thermometers and barometers used are based on the following exchange reactions between minerals:

Figure 1

	Partitioning	CPX	OPX	Olivine	Garnet
Thermometers					
T_BKN	Enstatite Component	X	X		
T_Ca	Ca		X		
T_Na	Na	X	X		
T_O'Neill	Fe-Mg			X	X
T_Krogh	Fe-Mg	X			X
T_NT	Enstatite Component	X			
Barometers					
P_BKN	Al		X		X
P_KB	Ca	X		X	
P_NT	Cr	X			X

*CPX=clinopyroxene; OPX=orthopyroxene; T_BKN=(Brey, Kohler, and Nickel, 1990); T_Ca=Calcium thermometer in (Brey, Kohler and Nickel, 1990); T_Na=Sodium thermometer in (Brey, Kohler, and Nickel, 1990); T_O'Neill=(O'Neill and Wood, 1979); T_Krogh=(Krogh, 1988); T_NT=(Nimis and Taylor, 2000); P_BKN=(Brey, Kohler, and Nickel, 1990); P_KB=(Kohler and Brey, 1990); and P_NT=(Nimis and Taylor, 2000)

The thermometers and barometers above were iteratively solved in the following combinations to calculate pressures and temperatures of equilibration:

I. T_BKN & P_BKN; T_Ca & P_BKN; T_Na & P_BKN

II. T_BKN & P_KB; T_Ca & P_KB; T_Na & P_KB

III. T_Krogh & P_BKN; T_Ca & P_BKN; T_Na & P_BKN

IV. T_O'Neill and Wood & P_BKN

V. T_NT & P_NT

These data were plotted and overlain with the best-fit geotherm of Rudnick and Nyblade (1999), as well as the mantle adiabat, in Figures 2 and 3.

Dodson Model Calculations

Calculations were made using Dodson's model for closure temperature depending on cooling rate and grain size (3). Temperatures were calculated using

$$\frac{E}{RTc} = \ln\left(\frac{\frac{ARTc^2Do}{a^2EdT}}{dt}\right) \qquad (3)$$

Fe-Mg diffusion coefficients for infinite temperature. Cooling rates of 1 degree/ Myr, 10 degrees/Myr, and 100 degrees/Myr were used in combination with mineral radii of 1E-3 m, 1E-4 m, and 1E-5 m. Such calculations were conducted for garnet, cpx, olivine, and opx to determine closure temperatures. Because calcium is pressure-dependent, diffusion of calcium is a good proxy for pressure variation at depth. These pressures were determined in a two-step process. First, closure temperatures for Ca-Mg exchange were calculated using Dodson's model (3). Then, pressures were calculated using Rudnick and Nyblade's geotherm. The temperatures from Fe-Mg exchange were used in conjuction with the Ca-Mg pressures to plot the estimations of the geotherm based on each mineral's diffusion coefficients. Linear and second-order polynomial fits were used to show the deviation of the calculated data from the geotherm.

Diffusion Modeling

Cation exchange across two and four phase mineral assemblages is modeled using finite difference methods modified from Neogi, Bolton, and Chakraborty (2008).

The forward model requires three input parameters: an initial pressure and temperature at depth as well as the ratio of Fe:Mg in olivine. From this information, the

starting compositions of the opx, cpx, and garnet are calculated based on partition coefficients (K_D's) from Brey and Kohler (1990) such that the initial state of the system is in equilibrium. The purpose of the model is to calculate how the chemical compositions in each mineral will change as time passes and the samples ascend to the surface. In order to make these calculations, the forward model uses Rudnick and Nyblade's geotherm to determine profiles of pressure and temperature as a function of depth, where depth is time-dependent. The pressure and temperature relationships are used to determine diffusion and partition coefficients, which are the essential parameters for defining boundary conditions and predicting changes in cation concentrations across mineral grains. As time evolves, the concentration of the chemical species from the core to the rim of each mineral is updated based on the modifications at the boundary between minerals. The model is run under ascent velocities of 1.0E-5, 1.0E-3, and 1.0E-2 meters per second and various grain sizes (e.g. 1E-3 m, 1E-4 m, and 1E-5 m) in order to determine the speed of ascent necessary for chemical diffusion to play a significant role in changing the pressures and temperatures obtained through thermobarometry.

The results of each run, defined using the same initial pressure, temperature, and composition but unique ascent velocities, are then put into the inverse model. The compositional data measured in this study are also put into the inverse model, which calculates K_D's using the formula defined by Brey and Kohler (1990):

$$K_D = [(X_1 / X_2)^A / (X_1 / X_2)^B] \qquad (2)$$

X is the mole fraction of element 1 or 2 determined for minerals A and B. Using two K_D's (one from coexistence of mineral A and B and a second from the coexistence of mineral B and C) and a second formula (3) defined by Brey and Kohler (1990) for ideal

systems, two equations (3) are defined and pressures and temperatures of equilibration are determined.

$$-RT\ ln\ K_D = \Delta H - T\Delta S + P\Delta V \qquad (3)$$

Pending the completion of the model, the results of the inverse problem will be plotted in relation to Rudnick and Nyblade's geotherm. A critical component of the forward and inverse methods is the solutions' dependence on the input parameters used in the initial stages of the forward model, e.g. ascent velocities and grain sizes.

Results

Electron Microprobe

Data from EPMA is attached in tables 1-11 of the appendix. Tables 1-8 contain data for core and rim measurements of thirty three garnet assemblages, and tables 9-11 include compositions from traverses taken across three garnets. The three traverses measure a clinopyroxene—garnet traverse (BU 6); an olivine—garnet—orthopyroxene transect (BU 21); and an olivine—garnet—olivine assemblage (BU 29).

--include some average compositions

Geothermobarometry

The electron microprobe data was used to calculate pressures and temperatures of equilibration at depth for the cores and rims of the garnets. These results are presented in Figure 2 and Figure 3. Most of the core data plots such that it is bisected by Rudnick and Nyblade's geotherm. The results derived from the Kohler and Brey barometer (P_{KB}) show a steeper trend, resulting in the highest pressure data obtained. The findings from the Krogh thermometer solved simultaneously with Brey, Kohler, and Nickel's $T_{Ca\text{-}in\text{-}OPX}$

(T1) and with $T_{Ni\text{-}btwn\ OPX/CPX}$ (T2) show significantly lower pressure data. However, the slope obtained is similar to the general trend of the data, as compared to steep slope of the P_{KB}—T_{BKN}, P_{KB}—T1, and P_{KB}—T2 results.

Dodson Calculations

The results from Dodson calculations are plotted below with Rudnick and Nyblade's geotherm. The temperatures used for each cooling rate at various grain sizes are determined using the Fe-Mg exchange in each of the minerals considered. The pressures obtained for opx, olivine, and garnet use Ca-(Mg/Fe) interdiffusion in garnet. From the closure temperatures calculated for Ca-(Mg/Fe), pressures are obtained using Rudnick and Nyblade's geotherm. These pressures are plotted with the temperatures derived from Fe-Mg exchange. The pressures for cpx are found using the Ca-Mg exchange in cpx.

The results for garnet and cpx are also plotted together with the geotherm. Linear trend lines are added in Figure 9 and second-order polynomial trend lines are added in Figure 10.

Figure 2

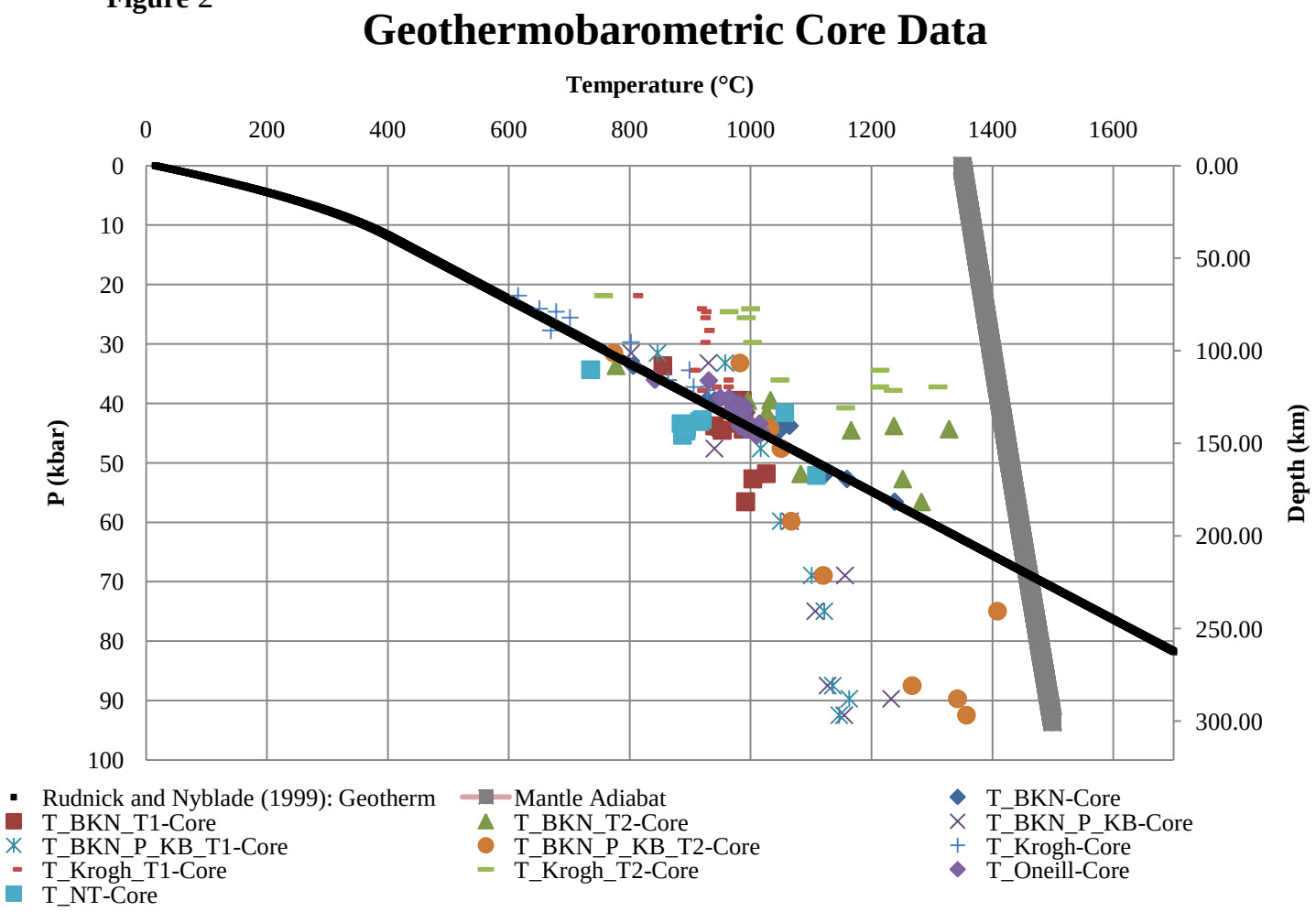
Geothermobarometric Core Data
Temperature (°C)
0
200
400
600
800
1000
1200
1400
1600
P (kbar)
0
10
20
30
40
50
60
70
80
90
100
Depth (km)
0.00
50.00
100.00
150.00
200.00
250.00
300.00
Rudnick and Nyblade (1999): Geotherm
Mantle Adiabat
T_BKN-Core
T_BKN_T1-Core
T_BKN_T2-Core
T_BKN_P_KB-Core
T_BKN_P_KB_T1-Core
T_BKN_P_KB_T2-Core
T_Krogh-Core
T_Krogh_T1-Core
T_Krogh_T2-Core
T_Oneill-Core
T_NT-Core

Figure 3

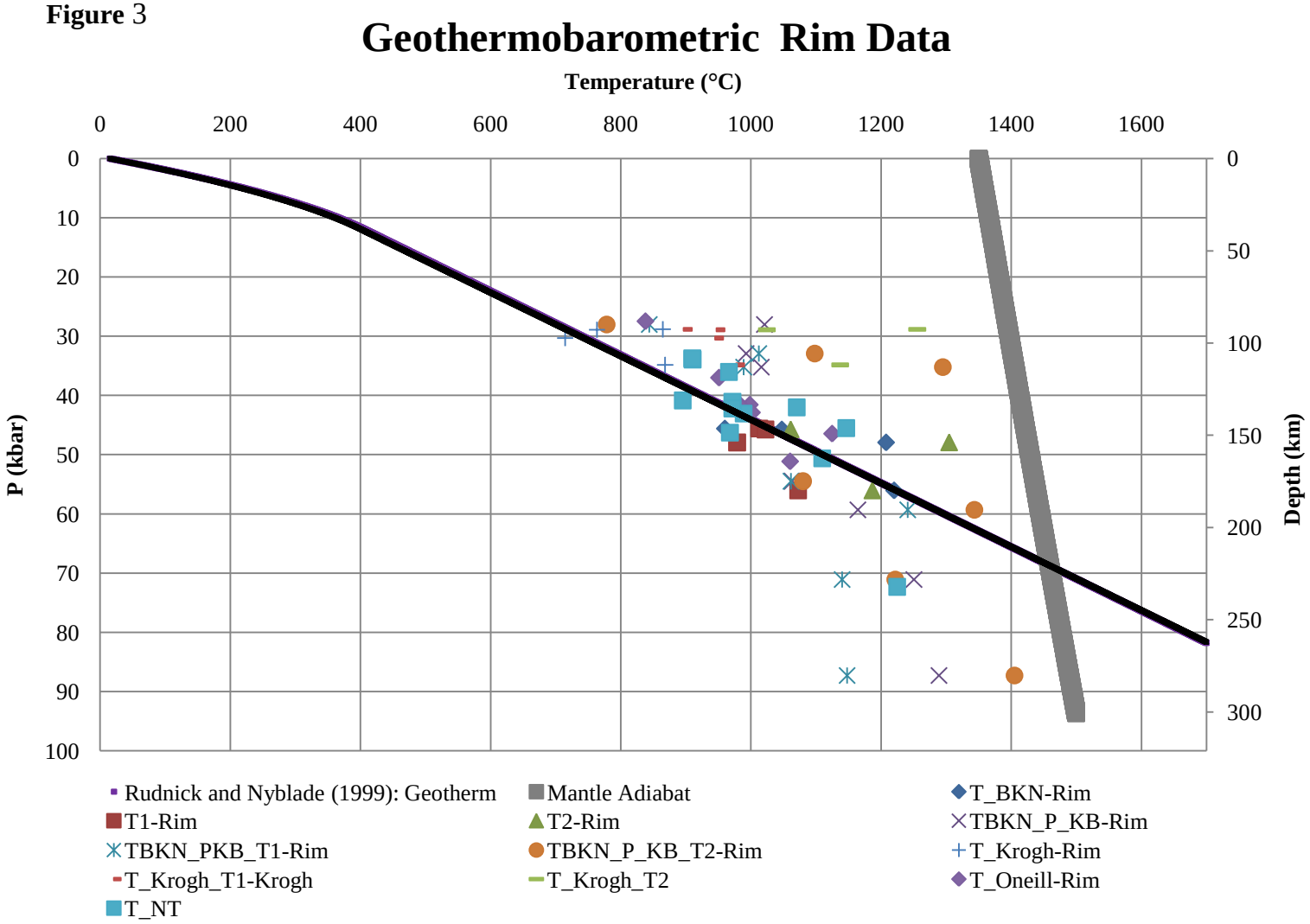
Geothermobarometric Rim Data
Temperature (°C)
0
200
400
600
800
1000
1200
1400
1600
P (kbar)
0
10
20
30
40
50
60
70
80
90
100
Depth (km)
0
50
100
150
200
250
300
Rudnick and Nyblade (1999): Geotherm
Mantle Adiabat
T_BKN-Rim
T1-Rim
T2-Rim
TBKN_P_KB-Rim
TBKN_PKB_T1-Rim
TBKN_P_KB_T2-Rim
T_Krogh-Rim
T_Krogh_T1-Krogh
T_Krogh_T2
T_Oneill-Rim
T_NT

Figure 4

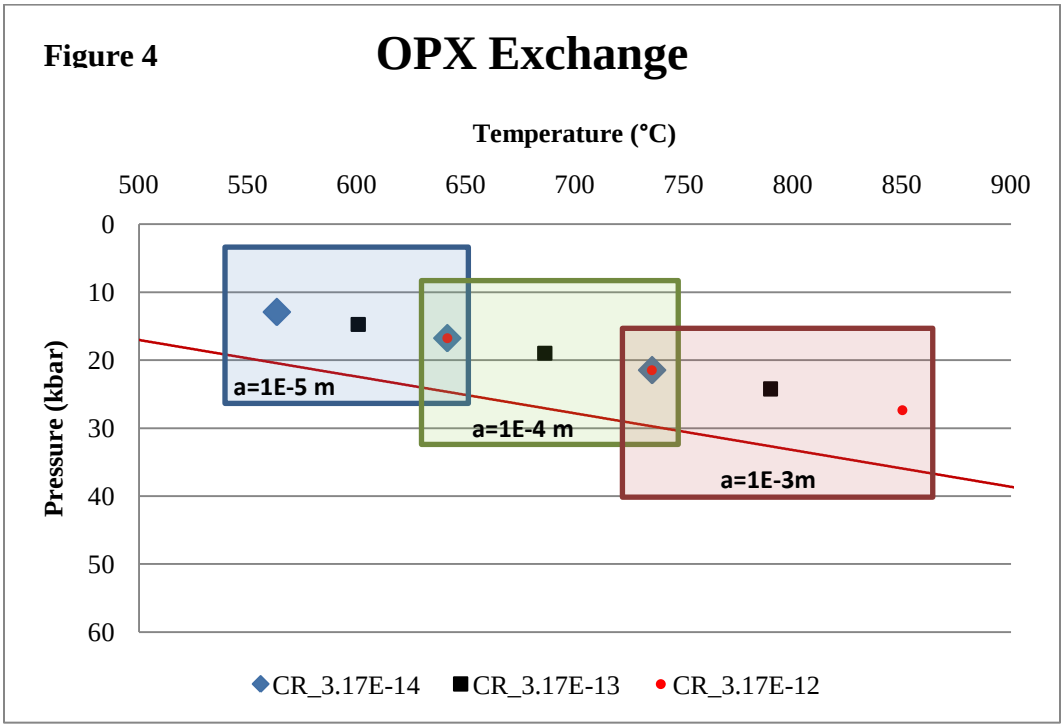

CR=Cooling Rate in degrees/second; 3.17E-14 deg/s=1deg/Myr.
A=mineral radius in meters

Figure 5

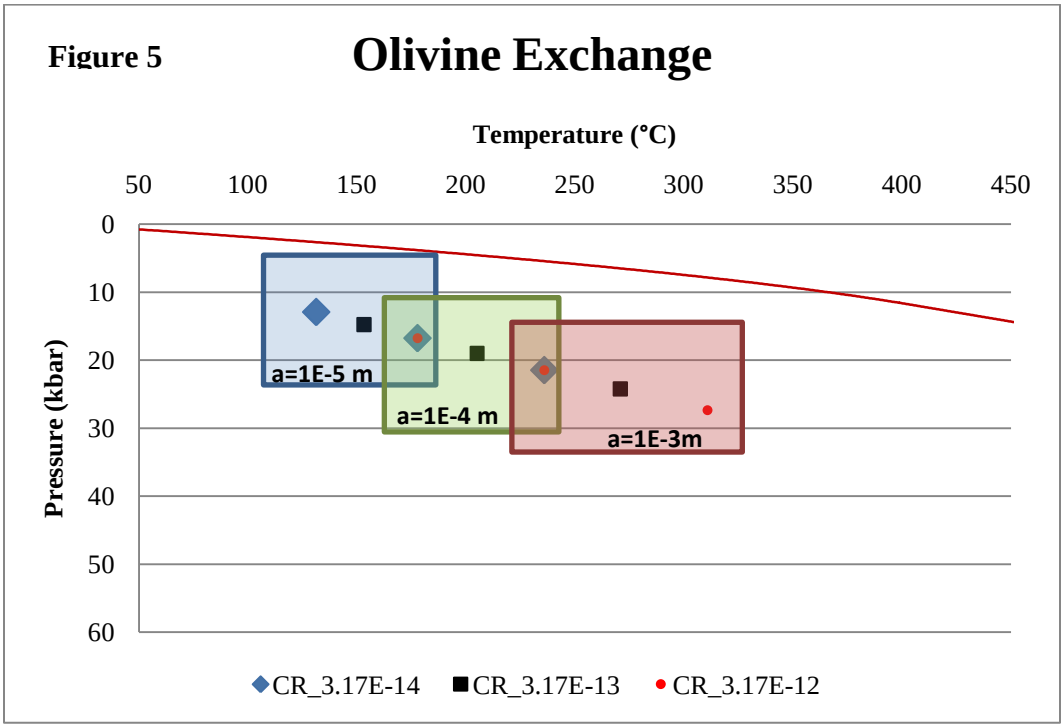

Figure 6

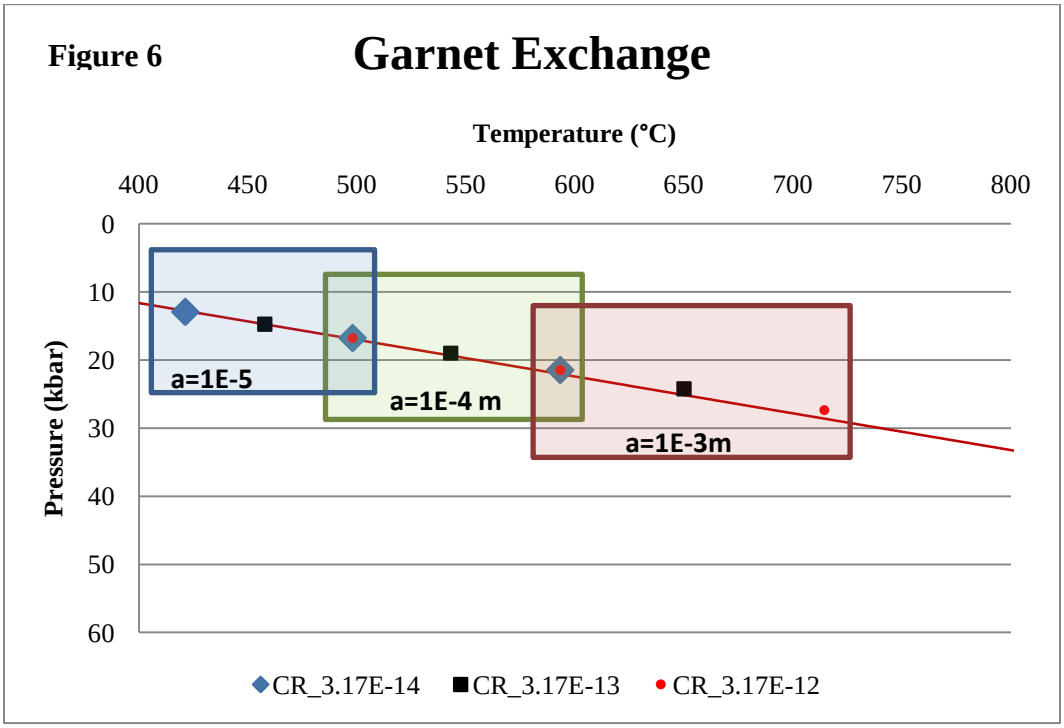

Figure 7

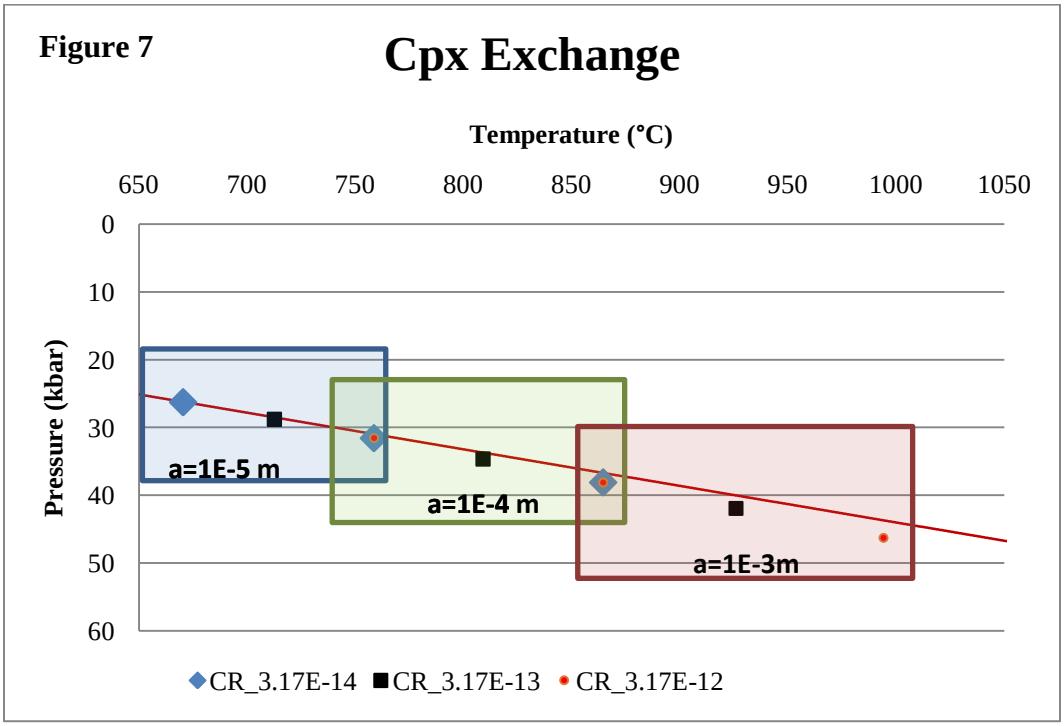

Figure 8

CPX and GRT Comparison to Geotherm: No Fits

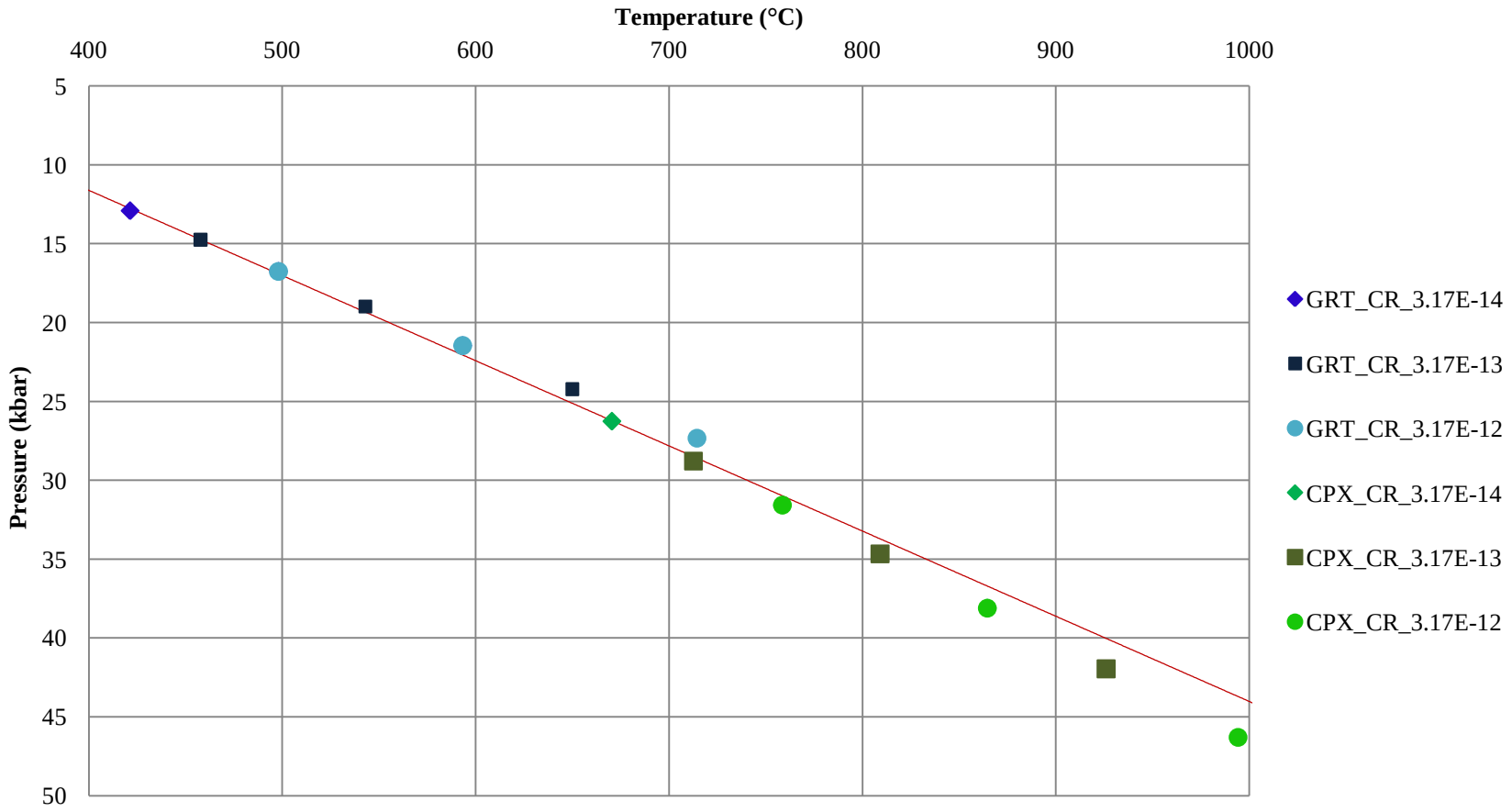

Figure 9 **CPX and GRT: Comparison to Geotherm with Linear Fits**

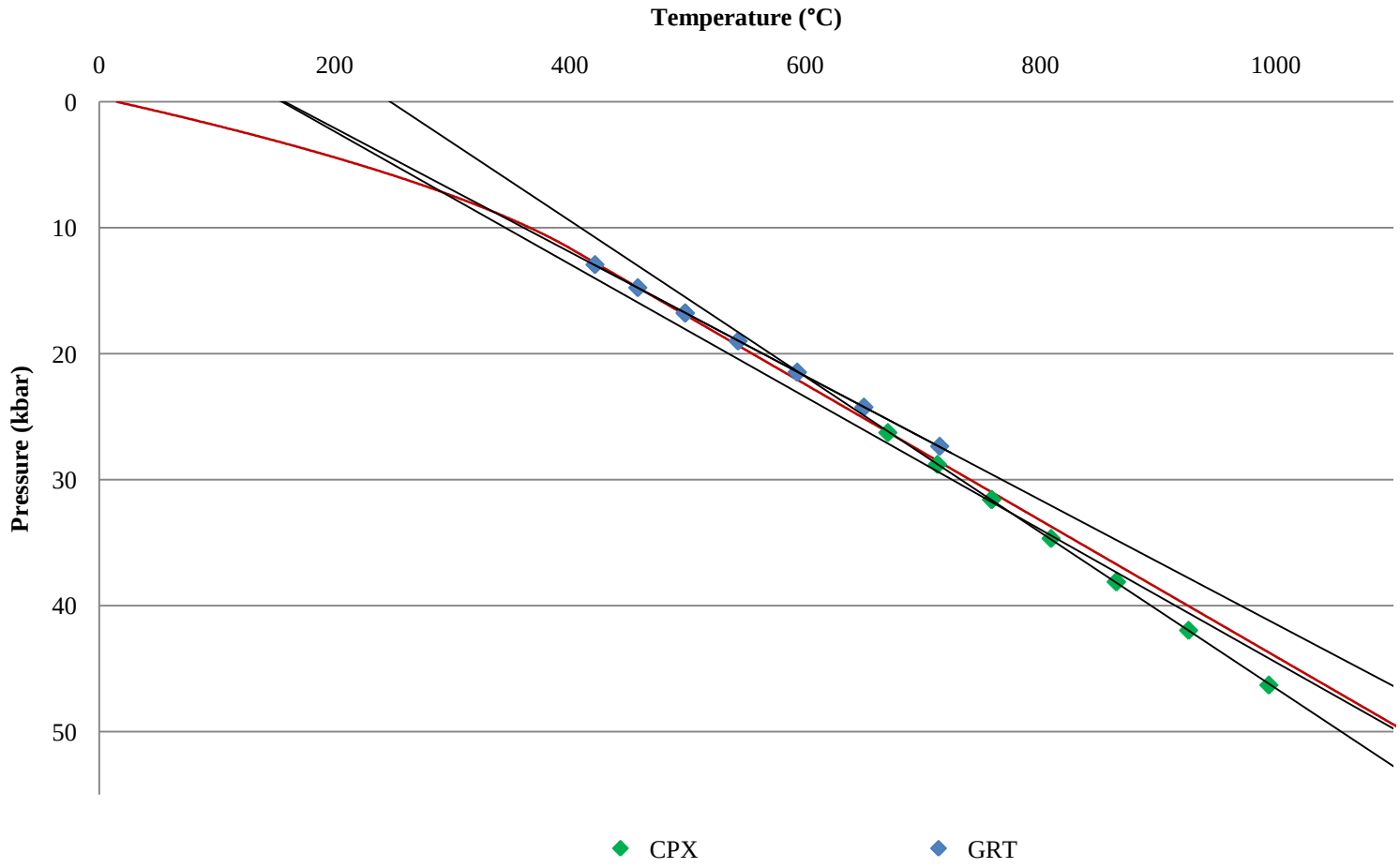

Figure 10 **CPX and GRT: Comparison to Geotherm with Polynomial Fits**

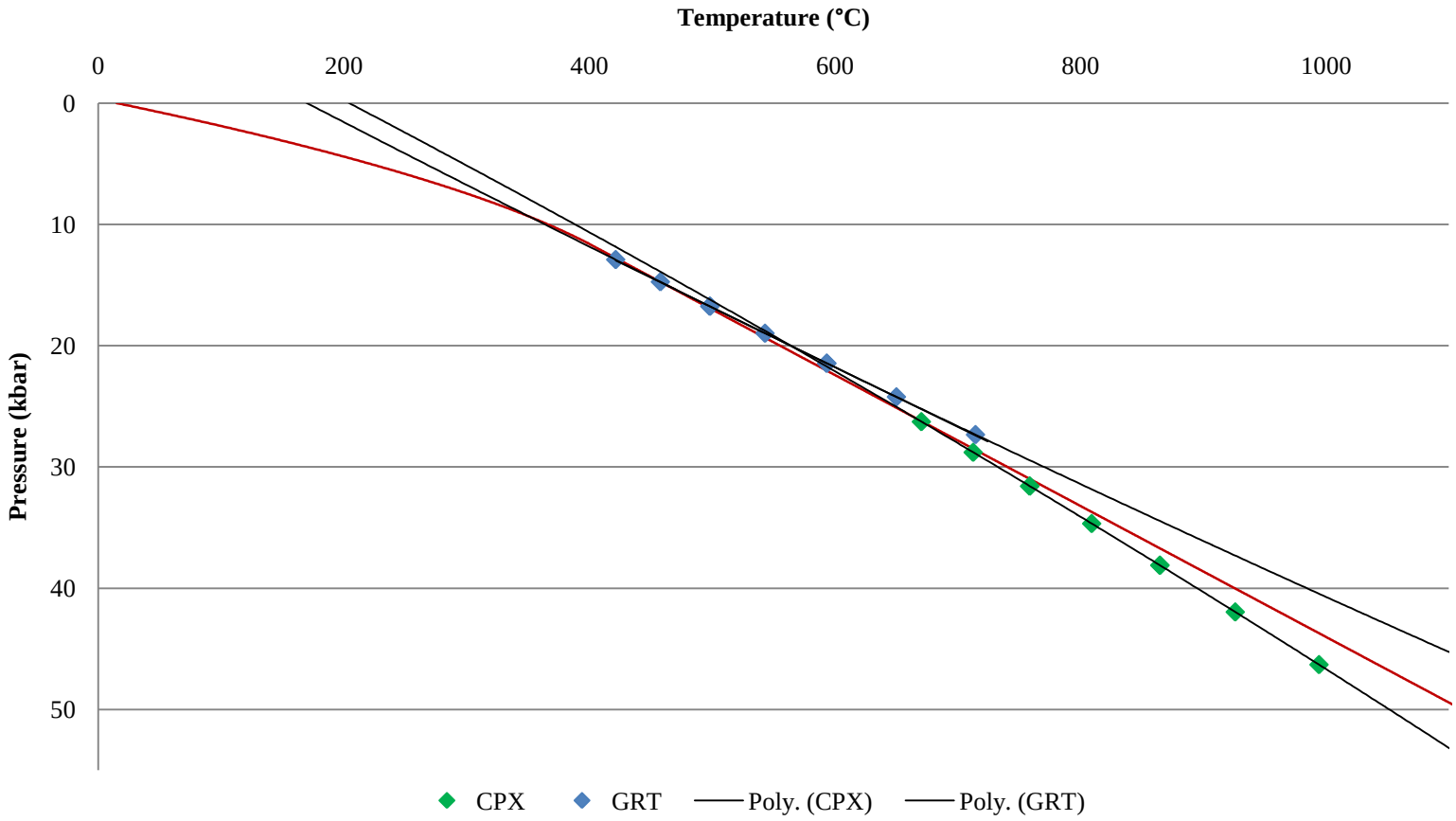

Diffusion Modeling

The results from the diffusion model are pending. After the successful addition of calcium in the model, the data will show calculated P-T conditions and will be plotted with Rudnick and Nyblade's 1999 geotherm.

Discussion

Since the pioneering work of Boyd in his 1973 paper "A Pyroxene Geotherm," many geothermobarometric models have been created to predict the equilibrium pressures and temperatures of mantle xenoliths. Thus, there is a vast number of models in the literature that use unique cation exchange between various minerals to predict these pressures and temperatures. Such data is important in the attempt to understand the earth's thermal history because the P-T results are linked to the geotherm, the best estimate of temperature variation at depth during Archean time. Understanding the curvature of the geotherm defines a heat flux from the mantle, which is an important parameter for understanding mantle convection and the many processes that result from this phenomenon.

The best estimate of the geotherm in the literature today is presented by Rudnick and Nyblade (1999). This model uses various parameters to find a geotherm that is closest to the best fit line of the calculated thermobarometric P-T data. The calculations made in this study show that Rudnick and Nybalde's best fit model may not represent the most accurate geotherm. Using the Dodson model, closure temperatures for garnet, cpx, opx, and olivine were calculated depending on cooling rate and grain size. Because cations diffuse at different rates in each mineral, a range of closure temperatures is

established for the exchanges within every mineral. Given calcium's sensitivity to pressure and the closure temperature of Ca-Mg exchange reactions, closure pressures were generated by solving Rudnick and Nyblade's geothermal gradient equation. For olivine and opx, the results deviate significantly from the geotherm. Olivine is especially a poor recorder of original conditions because cations are diffused very quickly and remnants of past conditions are easily re-equilibrated.

The results from the Dodson calculations show that garnet and cpx yield data close to the geotherm. However, there are two problems that arise if you take the best fit line as the most accurate geotherm. First, the profiles from garnet and cpx diverge from the best-fit line. Since the garnet data diverges above the temperature gradient, the geotherm is too low of an estimate of the temperature profile that would be expected based on the exchanges in garnet. The cpx data diverges below the geotherm, which implies an overestimation of the geotherm based on the projected profile from cpx. Given the unique diffusion coefficients defined for garnet and cpx, the results from one of the minerals is more likely to record the actual temperature profile with depth. Thus, taking the average of the results does not predict the most accurate temperature profile at depth as such an average would skew the profile from the most accurate data available. The geotherm that is most similar to the conditions at depth in the earth would follow the P-T path defined by the exchange recorded in the mineral with the slowest diffusion rates.

For this system, the diffusion coefficient for infinite temperature used for Fe-Mg exchange in garnet was 5.6E-8 m^2/s from Cygan and Lasaga (1983). The respective diffusion coefficient used for Fe-Mg exchange in cpx was 9.55E-5 m^2/s from Dimanov

and Sautler (2000). Thus, Fe-Mg exchange in garnets is slower than the same exchange in cpx by three orders of magnitude. Because Fe-Mg exchange is independent of pressure, the variation in the diffusion coefficients suggests that thermometers based on Fe-Mg exchange in garnet will be more accurate than thermometers based on this exchange in cpx. However, the diffusion coefficient for Fe-Mg exchange in garnet is not very well constrained. The four models in the literature for Fe-Mg diffusion coefficients in garnet of various compositions under different P-T conditions vary from 6.11E-4 m^2/s (Freer, 1981) to 2.3E-6 (Elphick et. al., 1981) to 5.6E-8 m^2/s (Cygan and Lasaga) and 5E-10 m^2/s (Duckworth and Freer, 1981). Given such a vast discrepancy in diffusion coefficients for garnet that range from slightly faster than cpx to five orders of magnitude slower, it is difficult to confidently say that the garnet profile is the most accurate. However, as diffusion coefficients become increasingly well understood, it should be simple to determine which exchanges record the most accurate temperature gradients.

The second problem with the best fit model is that the divergence between the calculations for each mineral is accentuated at higher temperatures and pressures. At pressures greater than 30 kbar, the divergence is significant enough that the curvature of the geotherm would have to be modified to account for the difference in data as compared to the average line. Because the curvature of the geotherm changes with the parameter for the heat flux of the mantle, it is one of the most important aspects of the temperature profile and must be defined as accurately as possible. The main motivation for obtaining geothermal gradients is to further our understanding of the thermal history of the earth. By defining the curvature in a more meaningful way, the geotherm will more successfully define the heat flux from the mantle. This is a very important

parameter for models of mantle convection, the process that either governs or influences almost all of earth's processes.

The results from the Dodson calculations show the effects of both cooling rate and grain size on the geotherm. In figures 4-7, the effect of differing mineral radii is apparent in the temperatures and pressures recorded. As the minerals increase in radius, they record higher temperatures and pressures. This is because it takes longer for the cores of the minerals to fully equilibrate with the melt or with the other phases with which it is in contact, resulting in a record of deeper and hotter conditions.

Cooling rate is also considered in the data plotted in figures 4-7. The data show that faster cooling rates result in higher P-T records. This is possible because the initial conditions were very hot and deep. Diffusion will occur at the cooling rate (degrees per second) for an allotted amount of time. If the cooling rate is faster, then the timescale over which cooling and diffusion occur will be shorter and conditions closer to the original state will be recorded.

The Dodson method shows that a more quantitative study of diffusion is necessary to determine changes in the input parameter of the geotherm. Such analysis is ongoing in the diffusion model constructed in this study. The framework of the three-element and four-phase diffusion model has been established, and the addition of the third element to the system is the final constraint for the success of the model. The results of the inverse step of the model will further demonstrate whether diffusion is a significant factor in determining the geotherm.

If the final pressures and temperatures calculated lie on the geotherm as defined by Rudnick and Nyblade, then diffusion does not matter. However, the results from the

Dodson calculations suggest that this will not be the case. The results obtained so far indicate that the data from the model will plot either below or above the geotherm and will determine whether or not the geotherm is an overestimate or underestimate of the most accurate temperature profile at depth.

Summary

Geothermal gradients provide important information for constraining the heat flux from the mantle of the earth. The current models in the literature provide different methods for assessing the temperature profile at depth in the lithospheric mantle. The most accepted of these models today, the geotherm by Rudnick and Nyblade (1999) may not constrain thermobarometric data in the most accurate way. The P-T data generated by thermobarometry is dependent on many exchange reactions with significantly different rates of diffusion. Comparisons of the data derived from these various thermobarometers are used in the geothermal models proposed in the literature, but the various thermobarometers record different pressures and temperatures based on the rates of cation diffusion. The best fit geotherm of Rudnick and Nyblade (1999) averages all the data, regardless of the type of cation exchange modeled. This study uses Dodson's model of closure temperatures to show that in order to produce the most accurate P-T data, diffusion determines which cation exchanges should be modeled by thermobarometry in order to define the geotherm. This study also includes the framework of a diffusion model to further investigate diffusion's role in the determination of the geotherm.

Acknowledgments

This project would not have been possible without the help and guidance of Zhengrong Wang and Ed Bolton. I am very grateful to both for their significant contributions and guidance. In addition, thanks to Jim Eckert for help with obtaining electron microprobe data and thanks to Brian Skinner for providing the Kimberlite samples.

References Cited

Basson I.J. and Viola G. (2004) Passive kimberlite intrusion into actively dilating dyke-fracture arrays: evidence from fibrous calcite veins and extensional fracture cleavage. *Lithos* **76**, 283-297.

Bercovici, D. (2003) The generation of plate tectonics from mantle convection. *Earth Planet. Sci. Lett.* **205**, 107-121.

Bercovici, D., Ricard, Y., and Richards, M.A. (2000) The relation between mantle dynamics and plate tectonics: A primer, in: M.A. Richards, R. Gordon, R. van der Hilst (Eds.), *History and Dynamics of Global Plate Motions, Geophys. Monogr. Ser.*, **121**, AGU, Washington, DC, 2000, pp. 5–46.

Berman, R.G. (1987) Internally-Consistent Thermodynamic Data for Minerals in the System Na2O-K2O-CaO-MgO-FeO-Fe2O3-Al2O3-SiO2-TiO2-H2O-CO2. *J. Petrol.* **29**, 445-522.

Boyd, F. R. (1973) A pyroxene geotherm. *Geochem. Cosmochim. Acta* **37**, 2533-2546.

Boyd, F.R. (1997) Composition of the Siberian cratonic mantle: evidence from Udachnaya peridotite xenoliths. *Contrib. Mineral. Petrol.* **128**, 228-246.

Brady, J.B. and McCallister, R.H. Diffusion data for clinopyroxenes from homogenization and self-diffusion experiments. *American Mineralogist*, **68**, 95-105.

Canil, D., Fedortchouk, Y. (1999) Garnet dissolution and the emplacement of kimberlites. *Earth and Planetary Science Letter* **167**, 227-237.

Carlson, R.W., Pearson, D.G., Boyd, F.R., Shirey, S.B., Irvine, G., Menzies, A.H., and Gurney, J.J. (1999) Re-Os systematic of lithospheric peridotites: implications for lithosphere formation and preservation, in *Proc. VIIth International Kimberlite Conference, B.J. Dawson Volume*, edited by J.J. Gurney, J.L. Gurney, M.D. Pascoe, and S.R. Richardson, 99-108.

Cygan,R. T. and Lasaga,A. C. (1983) Self-diffusion magnesium in garnet at 750-900'C. *Geological Society of America Abstracts with Programs*, **15**, 552.

Dimanov, A. and Sautter, V. (2000) "Average" interdiffusion of (Fe,Mn)-Mg in natural diopside. *Eur. J. Mineral.* **12**, 749-760.

Dodson, M.H. (1973) Closure Temperature in Cooling Geochronological and Petrological Systems. *Contrib. to Mineral. And Petrol.* **40**, 259-274.

Duckworth, S. and Freer, R. (1981) Cation diffusion studies in garnet-garnet and garnet-pyroxene couples at high temperatures and pressures. In Ford, C. 8., Ed. Progress in Experimental Petrology, *The Natural Environment Research Council Publications Series D*, **18**, 36-39. Eaton Press,Wallasey, G. B.

Elphick, S. C., Ganguly,J., and Loomis, T. P. (1981) Experimental study of Fe-Mg interdiffusion in aluminumsilicate garnet. *Transactions American Geophysical Union (EOS)* **62**, 4l1.

Finnerty A.A. and Boyd F.R. (1984) Evaluation of thermometers for garnet peridotites. *Geochemica et Cosmochemica Acta* **48**, 15-27.

Freer, R. (1981) Diffusion in silicate minerals and glasses: a data digest and guide to the literature. *Contrib. to Mineral. and Petrol.*, **76**, 440-454.

Freer, R. and Edwards, A. (1999) An experimental study of Ca-(Fe,Mg) interdiffusion in silicate garnets. *Contrib. to Mineral. Petrol.*

Ganguly, J. (1981) Order-disorder kinetics of ferromagnetism silicates, and the cooling history of rocks. *EOS Transactions on the American Geophysical Union* **62**, 414.

Gurnis M. (1988) Large-scale mantle convection and the aggregation and dispersal of supercontinents. *Nature* **332**, 695-699.

Hager, B., and O'Connell R. (1981). A Simple Global Model of Plate Dynamics and Mantle Convection, *J. Geophys. Res.* **86(B6)**, 4843-4867.

Hoffman, P.F. (1988) United plates of America, the birth of a craton: early Proterozoic assembly and growth of Laurentia. *Ann. Rev. Earth Planet. Sci.* **16**, 543-603.

Hoffman, P.F. (1989) Precambrian geology and tectonic history of North America, in *The geology of North America-An Overview*, edited by B.A. W., and A.R. Palmer, 447-511, Geological Society of America, Boulder, CO.

Kopylova, M.G., Russell, J.K., and Cookenboo, H. (1999) Petrology of Peridotite and Pyroxenite Xenoliths for the Thermal State of the Mantle beneath the Slave Craton, Northern Canada. *J. Petrology*, **40**, 79-104.

Lee, C.A. Geochemical/ Petrologic Constraints on the Origin of Cratonic Mantle. In *Archean geodynamics and environments*, edited by K. Benn, J. Mareschal, and K.C. Condie, 89-114.

McCallister, R.H., Meyer, H.O.A. and Aragon, R. (1979) Partial thermal history of two exolved clinopyroxenes from the Thaba Putsoa kimberlite pipe, Lesotho. *Proceedings of the Second International Kimberlite Conference. American Geophysical Union, Washington, D.C.*, 244-247.

McGetchin T. R. (1968) The Moses Rock Dyke: geology, petrology and mode of emplacement of a kimberlite-bearing brecia, San Juan County, Utah. PhD thesis, CalTech.

McGetchin T.R. and Ullrich, G.W. (1973) Xenoliths in maars and diatremes, with inferences for the moon, Mars and Venus. *J. Geophys. Res.* **78**, 1832-1852.

Mercier, C.C. (1979) Peridotite xenoliths and the dynamics of kimberlite intrusion. In: F.R. Boyd and H.A.O. Meyer, Editors, *The Mantle Sample*, American Geophysical Union, Washington, DC, 1971.

Michaut C., Jaupart C., and Bell, D.R. (2007) Transient geotherms in Archean continental lithosphere: New constraints on thickness and heat production of the subcontinental lithospheric mantle. *J. Gepohys. Res*. **112**, B04408, doi:10.1029/2006JB004464.

Mitchell, R.H. (1971) Kimberlite–xenolith interactions Abstracts Kimberlite Symposium II, Cambridge, July 1979.

Morgan P. (1984) The Thermal Structure and Thermal Evolution of the Continental Lithosphere. *Phys. and Chem. of the Earth* **15,** 107-193.

Neogi, S., Bolton, E.W., and Chakraborty, S. (2008) Constraints on timescales of disequilibrium melting in the crust from trace element modelling: A case study of the formation and segregation of melts in the sillimanite zone, Sikkim Himalaya, *Contrib. Mineral. Petrol.*, (in Press).

Nyblade A.A. and Pollack H.N. (1993) A Global Analysis of Heat Flow From Precambrian Terrains: Implications for the Thermal Structure of Archean and Proterozoic Lithosphere. J. of Geophys. Res. **98**, 12, 207-212, 218.

O'Hara M.J., Richardson S.E., and Wilson G. (1971) Garnet peridotite stability and occurrence in crust and mantle. Contr. Min. Petrol. **32**, 48-68.

Pearson, D.G., Carlson, R.W. Shirley, S.B., Boyd, F.R., and Nixon, P.H. (1995a) Stabilization of Archean lithospheric mantle: a Re-Os isotope study of peridotite xenoliths from the Kaapvaal craton, *Earth Planet. Sci. Lett.* **134**, 341-357.

Pollack H.N. and Chapman D. S. (1977) On the regional variation of heat flow, geotherms, and lithospheric thickness. *Tectonophysics* **38**, 279-296.

Philpotts A., and Ague J.J. (2009) *Principles of Igneous and Metamorphic Petrology*. Cambridge University Press, New York, 667.

Pre, S., Wirr, G., Seck, H.A., Eonov, D., and Kovalenko, V.I. (1986) Spinel peridotite xenoliths from the Tariat Depression, Mongolia. I: Major element chemistry and mineralogy of a primitive mantle xenolith suite. *Geochemica et Cosmochemica Acta*, **50**, 2587-2599.

Richardson, S.H., Gurney, J.J., (1984) Erlank, A.J., and Harris, J.W. Origin of diamonds in old enriched mantle, *Nature* **310**, 198-202.

Rudnick R.L., and Nyblade A.A. (1999) The thickness and heat production of Archean lithosphere: constraints from xenoliths thermobarometry and surface heat flow. In (Fei, Y.-W., Bertka, C.M. and Mysen, B.O., eds.) *Mantle Petrology: Field Observations and High-Pressure Experimentation: A Tribute to Francis R. (Joe) Boyd*, Geochemical Soc. Spec. Publ. **6**, 3-12.

Rutherford M.J. and Gardener J.E. (2000) Rates of magma ascent. In: H. Sigurdsson, Editor, *Encyclopedia of Volcanoes*, Academic Press, San Diego, 207–217.

Ryan C.G., and Griffin W.L. (1996) Garnet geotherms: Pressure-temperature data from Cr-pyrope garnet xenocrysts in volcanic rocks. *J. Geophys. Res.* **101**, 5611-5625.

Santosh, M. (2010) A synopsis of recent conceptual models on supercontinent tectonics in relation to mantle dynamics, life evolution and surface environment. *J. Geodyn*. **50**, 116-133.

Schlater J.G., and Francheteau, J. (1970) The Implications of Terrestrial Heat Flow Obsevations on Current Tectonic and Geochemical Models of the Crust and Upper Mantle of the Earth. *Geophys. J. R. astr. Soc*. **20**, 509-542.

Smith, D. and Boyd, F.R. (1992) Compositional zonation in garnets in peridotite xenoliths. Contrib. Mineral. Petrol. **112**, 134-147.

Smith, D. and Wilson, C.R. (1985) Garnet-olivine equilibration during cooling in the mantle. American Mineralogist, 70, 30-39.

Smyth J.R. and Hatton, C.J. (1977) A coesite sanidine-grospydite from the Roberts Victor kimberlikte, *Earth and Planetary Science Letters* **34**, 284-290.

Spear, F.S. (1993) Metamorphic phase equilibria and pressure-temperature-time paths. *Mineralogical Society of America*, Washington D.C., 799.

Stille, H.W. (1936) The present tectonic state of the Earth. *Am. Assoc. Petroleum Geologists Bull.* **20**, 849-880.

Tackley, P.J. (1998) Self-consistent generation of tectonic plates in three-dimensional mantle convection, *Earth Planet. Sci. Lett.* **157**, 9–22.

Tackley P.J. (2000) Mantle Convection and Plate Tectonics: Toward an Integrated Physical and Chemical Theory. *Science* **288**, 2002-2007.

Walker, R.J., Carlson, R.W., Shirey, S.B., and Boyd, F.R. (1989) Os, Sr, Nd, and Pb isotope systematic of southern African peridotite xenoliths: implications for the chemical evolution of subcontinental mantle, *Geochem. Cosmochem*. **53**, 1583-1595.

Wilson L. and Head J.W. (2007) An integrated model of kimberlite ascent and eruption. *Nature*, **447**, 53-57.

Appendix

Table 1: Compositions of Garnet at Core

Sample	Garnet	SiO_2	TiO_2	Al_2O_3	Cr_2O_3	FeO	MnO	NiO	MgO	CaO	Na_2O	Total
BU 3	2	42.149	0.055	20.686	4.374	6.279	0.311	0.003	21.414	4.771	0.023	100.065
BU 3	3	42.465	0.058	20.813	4.334	6.271	0.297	0.008	21.503	4.797	0.034	100.580
BU 3	4	42.403	0.062	20.868	4.529	6.402	0.315	0.012	21.423	4.861	0.113	100.988
BU 3	1	42.310	0.063	20.819	4.397	6.412	0.300		21.504	4.720	0.048	100.573
BU 5	1	42.238		21.203	4.093	6.317	0.316	0.004	22.003	3.682	0.026	99.882
BU 5	2	41.885		20.669	4.446	6.187	0.312	0.013	21.972	3.772	0.010	99.266
BU 6	1a	41.973	0.037	20.590	4.299	6.853	0.331		20.694	5.287	0.023	100.087
BU 6	1b	41.814	0.042	20.632	4.274	6.908	0.312	0.016	20.727	5.207	0.015	99.947
BU 6	2	41.939	0.039	20.432	4.283	6.948	0.325	0.016	20.610	5.449	0.028	100.069
BU 6	3	41.824	0.043	20.451	4.321	6.967	0.327	0.001	20.674	5.418	0.016	100.042
BU 13	3	42.222	0.109	20.530	4.389	6.870	0.325	0.001	20.682	5.373	0.016	100.517
BU 13	2	42.191	0.105	20.610	4.218	6.775	0.330		20.657	5.345	0.020	100.251
BU 13	1	42.182	0.102	20.410	4.353	6.740	0.318		20.680	5.292	0.025	100.102
BU 18	1	42.710		21.148	4.174	6.660	0.304		21.173	5.419	0.020	101.608
BU 18	2	42.686		21.110	4.077	6.548	0.307	0.011	21.089	5.222	0.049	101.099
BU 18	4	42.406		20.991	4.177	6.633	0.304		21.080	5.225	0.029	100.845
BU 18	5	42.711		21.477	3.742	6.655	0.315	0.009	21.292	5.135	0.031	101.367
BU 18	6	42.719		21.400	3.825	6.615	0.326	0.006	21.188	5.313	0.019	101.411
BU 21	3	42.375		20.553	4.564	6.336	0.317	0.007	21.234	4.759	0.035	100.180
BU 21	1	42.097		20.794	4.324	6.242	0.321	0.004	21.191	4.752	0.040	99.765
BU 21	2	42.271		20.588	4.726	6.292	0.315		21.123	4.856	0.034	100.205
BU 25	3	42.175	0.017	21.537	3.447	6.568	0.330	0.002	21.297	4.820	0.013	100.206
BU 25	1	42.415	0.014	21.173	4.033	6.555	0.324		21.049	5.000	0.014	100.577

Table 1: Garnet, Core (continued)

Sample	Garnet	SiO_2	TiO_2	Al_2O_3	Cr_2O_3	FeO	MnO	NiO	MgO	CaO	Na_2O	Total
BU 25	2	42.409	0.013	21.265	3.876	6.511	0.336		21.087	5.142	0.006	100.645
BU 29	1	41.871	0.142	19.719	5.337	6.759	0.353		20.649	4.961	0.058	99.849
BU 29	2	42.314	0.151	19.689	5.603	6.801	0.353	0.018	20.722	5.196	0.042	100.889
BU 29	3	42.180	0.144	19.728	5.585	6.764	0.342	0.004	20.736	5.112	0.038	100.633
BU 29	4	42.171	0.139	19.922	5.289	6.785	0.350	0.012	20.719	5.013	0.035	100.435
BU 33	1	42.177	0.014	20.260	4.984	6.386	0.305		20.985	5.093	0.014	100.218
BU 33	2	42.225	0.017	20.364	4.819	6.342	0.317	0.001	21.148	5.067	0.024	100.324
BU 33	3	42.258	0.017	20.534	4.639	6.374	0.303	0.006	21.185	4.987	0.029	100.332
BU 33	4b	41.725	0.015	20.075	5.005	6.312	0.286	0.003	21.019	5.109	0.021	99.570
BU 34	1	42.338	0.049	22.502	2.034	9.258	0.467		19.936	4.553	0.010	101.147

Table 2: Compositions of Garnet at Rim

Sample	Garnet	SiO_2	TiO_2	Al_2O_3	Cr_2O_3	FeO	MnO	NiO	MgO	CaO	Na_2O	Total
BU 3	2	41.446	0.067	20.191	4.344	6.346	0.304		21.041	4.688	0.031	98.458
BU 3	4	43.068	0.075	21.080	4.287	6.325	0.300		21.969	4.611	0.034	101.749
BU 3	1	42.613	0.064	21.005	4.304	6.370	0.305	0.004	22.051	4.656	0.051	101.423
BU 5	2	42.244		20.596	4.874	6.339	0.301	0.024	21.876	3.860	0.028	100.142
BU 6	1a	42.240	0.043	20.824	4.276	6.926	0.335	0.008	20.963	5.203	0.017	100.835
BU 6	1b	41.419	0.044	20.237	4.296	6.925	0.328	0.020	20.334	5.212	0.023	98.838
BU 6	2	42.709	0.047	20.738	4.426	6.893	0.315	0.012	20.885	5.264	0.017	101.306
BU 6	3	43.012	0.041	21.077	4.322	6.936	0.317	0.014	21.116	5.194	0.019	102.048
BU 13	2	42.864	0.102	20.840	4.422	6.836	0.343	0.005	21.608	5.259	0.026	102.305

Table 2: Garnet, Rim (continued)

Sample	Garnet	SiO_2	TiO_2	Al_2O_3	Cr_2O_3	FeO	MnO	NiO	MgO	CaO	Na_2O	Total
BU 13	1	42.699	0.109	20.809	4.388	6.829	0.327	0.007	21.141	5.194	2.766	104.269
BU 18	1	43.044		21.390	3.919	6.650	0.305	0.010	20.762	5.137	0.009	101.226
BU 21	1	41.940	0.007	20.094	5.082	6.371	0.301		21.295	4.442	0.023	99.555
BU 21	1	42.318	0.015	20.655	4.509	6.298	0.304	0.022	21.784	4.105	0.057	100.067
BU 25	3	42.231	0.020	20.768	4.559	6.514	0.343		21.034	5.114	0.026	100.609
BU 25	2	42.530	0.014	20.835	4.432	6.524	0.318	0.009	20.928	5.108	0.018	100.716
BU 29	1	42.127	0.141	20.112	4.948	6.869	0.339	0.011	21.343	4.608	0.044	100.542
BU 29	2	42.891	0.151	20.100	5.423	6.822	0.349	0.008	21.188	4.784	0.044	101.760
BU 29	3	41.893	0.227	20.224	4.537	5.806	0.263	0.022	22.045	4.001	0.028	99.046
BU 33	1	41.987	0.012	20.167	4.968	6.364	0.313	0.010	21.085	5.027	0.020	99.953
BU 33	2	41.834	0.019	19.983	4.990	6.354	0.302		20.969	5.070	0.015	99.536
BU 33	3	42.054	0.019	20.217	4.991	6.408	0.314	0.002	21.028	5.046	0.022	100.101
BU 33	4	41.885	0.014	20.110	4.944	6.291	0.297	0.006	20.800	5.099	0.011	99.457

Table 3: Compositions of Clinopyroxene at Core

Sample	Garnet	SiO_2	TiO_2	Al_2O_3	Cr_2O_3	FeO	MnO	NiO	MgO	CaO	Na_2O	K_2O	Total
BU 5	2	54.140	0.481	0.331	0.96	2.552	0.103	0.036	18.810	20.575	0.966	0.005	98.959
BU 6	1a	54.615	0.017	1.566	1.525	2.037	0.072	0.056	17.207	21.232	1.538	0.008	99.873
BU 6	1b	54.377	0.012	1.600	1.502	2.125	0.071	0.067	17.120	21.054	1.557	0.005	99.490
BU 6	2	54.570	0.014	1.565	1.510	2.126	0.054	0.047	17.050	21.041	1.609	0.004	99.590
BU 6	3	54.430	0.019	1.582	1.532	2.131	0.073	0.063	17.120	21.040	1.570	0.008	99.568

Table 3: Cpx, Core (Continued)

Sample	Garnet	SiO_2	TiO_2	Al_2O_3	Cr_2O_3	FeO	MnO	NiO	MgO	CaO	Na_2O	K_2O	Total
BU 18	6	54.840		1.449	1.351	1.945	0.064	0.059	17.474	21.542	1.409	0.002	100.135
BU 25	1	54.901	0.358	1.620	0.404	2.902	0.144	0.034	18.298	20.393	1.156	0.002	100.212
BU 29	1	54.706	0.572	0.350	0.533	3.162	0.136	0.028	18.314	21.609	0.873	0.008	100.291
BU 29	4	55.497	0.111	2.685	2.480	2.409	0.066	0.043	16.081	18.882	2.791	0.010	101.055
BU 29	1	55.029	0.004	1.897	2.169	2.015	0.076	0.06	16.814	20.289	1.981	0.007	100.341
BU 33	3	54.817	0.332	1.959	0.639	2.650	0.105	0.039	18.215	20.799	1.170		100.725
BU 34	1	54.907	0.113	2.130	1.858	2.694	0.062	0.043	15.852	21.244	1.936	0.011	100.850

Table 4: Compositions of Clinopyroxene at Rim

Sample	Garnet	SiO_2	TiO_2	Al_2O_3	Cr_2O_3	FeO	MnO	NiO	MgO	CaO	Na_2O	K_2O	Total
BU 5	2	55.152	0.357	0.267	0.611	2.68	0.108	0.035	20.087	20.546	0.789	0.002	100.634
BU 6	1a	54.170	0.021	1.730	1.578	2.186	0.065	0.04	17.100	20.98	1.556	0.004	99.430
BU 6	1b	54.239	0.022	2.477	1.685	2.258	0.052	0.048	16.851	20.761	1.651	0.006	100.05
BU 6	2	55.115	0.016	1.763	1.613	2.165	0.062	0.052	17.457	20.766	1.518	0.012	100.539
BU 6	3	54.019	0.037	2.436	1.761	2.403	0.09	0.048	17.08	20.293	1.666	0.005	99.838
BU 18	6	55.753		1.624	1.369	2.101	0.072	0.061	17.719	21.238	1.508	0.003	101.448
BU 21	3	54.434	0.355	2.110	0.681	2.925	0.135	0.031	18.305	19.334	1.313	0.007	99.630
BU 21	1	52.829	0.705	4.372	1.296	2.683	0.108	0.035	16.192	20.447	1.655	0.002	100.324
BU 21	2	54.249	0.483	2.061	0.974	2.887	0.143	0.028	17.726	19.042	1.665	0.001	99.259
BU 25	1	54.614	0.488	2.066	0.499	2.883	0.138	0.039	17.982	20.353	1.240	0.004	100.306
BU 29	4	53.713	0.260	1.496	1.833	2.798	0.114	0.033	17.172	20.873	1.284		99.576
BU 33	1	55.068	0.023	1.986	2.130	2.097	0.069	0.043	16.917	20.089	1.898	0.008	100.328

BU 33	2	55.473	0.150	1.198	0.568	2.858	0.103	0.042	19.233	19.941	1.090	0.003	100.659
BU 34	1	54.807	0.109	3.723	1.831	3.419	0.112	0.028	15.055	18.528	2.792	0.002	100.406

Table 5: Compositions of Orthopyroxene at Core

Sample	Garnet	SiO_2	TiO_2	Al_2O_3	Cr_2O_3	FeO	MnO	NiO	MgO	CaO	Na_2O	K_2O	Total
BU 3	2	58.611	0.011	0.697	0.336	4.225	0.101	0.108	36.430	0.429	0.120		101.068
BU 3	4	58.620	0.015	0.659	0.321	4.236	0.097	0.117	36.000	0.414	0.153	0.001	100.633
BU 6	1a	58.009	0.003	0.607	0.279	4.522	0.104	0.113	36.208	0.439			100.284
BU 13	3	58.048	0.039	0.602	0.262	4.541	0.100	0.096	36.255	0.438	0.082		100.463
BU 18	2	58.388		0.619	0.272	4.417	0.091	0.104	36.495	0.452	0.107	0.002	100.947
BU 18	4	58.533		0.601	0.254	4.398	0.095	0.115	36.642	0.446	0.098	0.002	101.184
BU 18	6	58.834		0.637	0.274	4.520	0.106	0.106	36.469	0.453	0.077	0.006	101.482
BU 21	3	58.016	0.003	0.714	0.405	4.147	0.102	0.109	35.826	0.334	0.145		99.801
BU 21	1	58.394		0.658	0.391	4.131	0.107	0.102	36.460	0.353	0.140	0.002	100.738
BU 21	2	58.826		0.635	0.367	4.116	0.091	0.110	36.215	0.333	0.168		100.861
BU 25	3	58.611		0.580	0.318	4.362	0.096	0.106	36.401	0.421	0.108	0.003	101.006
BU 25	1	58.631	0.002	0.621	0.326	4.355	0.109	0.101	36.729	0.383	0.124		101.381
BU 25	2	58.185	0.004	0.644	0.332	4.387	0.103	0.194	36.301	0.389	0.096	0.001	100.636
BU 29	1	58.289	0.040	0.673	0.376	4.603	0.117	0.109	36.069	0.420	0.134		100.830
BU 29	4	59.027	0.044	0.675	0.378	4.603	0.121	0.112	36.078	0.412	0.146		101.596
BU 33	1	58.373		0.669	0.366	4.286	0.085	0.120	36.149	0.448	0.103	0.001	100.600
BU 33	3	58.854	0.002	0.663	0.368	4.381	0.105	0.120	36.323	0.433	0.069		101.318
BU 33	4b	58.555		0.649	0.359	4.230	0.098	0.118	36.586	0.436	0.111		101.142
BU 34	1	58.210	0.045	0.631	0.200	5.840	0.123	0.086	35.563	0.264	0.040		101.002

Table 6: Compositions of Orthopyroxene at Rim

Sample	Garnet	SiO_2	TiO_2	Al_2O_3	Cr_2O_3	FeO	MnO	NiO	MgO	CaO	Na_2O	K_2O	Total
BU 3	3	58.345	0.018	0.738	0.409	4.286	0.096	0.111	35.757	0.000	0.133		100.367
BU 3	4	57.825	0.013	0.739	0.397	4.224	0.093	0.113	35.161	0.438	0.096	0.006	99.105
BU 6	1a	58.297	0.009	0.633	0.303	4.499	0.095	0.119	36.580	0.461	0.000		100.996
BU 6	3	57.887	0.011	0.660	0.327	4.718	0.106	0.108	35.825	0.476	0.095		100.213
BU 13	1	57.676	0.031	0.637	0.355	4.526	0.090	0.114	35.860	0.478	0.049		99.816
BU 18	1	58.687		0.638	0.258	4.590	0.089	0.108	36.790	0.447	0.078		101.685
BU 18	2	58.130	0.022	1.252	0.457	4.501	0.104	0.109	35.814	0.606	0.117	0.006	101.118
BU 18	4	59.734		0.643	0.279	4.517	0.095	0.119	37.288	0.447	0.082		103.204
BU 18	5	58.163	0.028	1.106	0.434	4.592	0.102	0.101	36.082	0.578	0.117		101.303
BU 18	6	58.451	0.023	1.131	0.415	4.551	0.107	0.117	36.407	0.601	0.109		101.912
BU 21	3	58.083		0.869	0.473	4.338	0.111	0.098	35.747	0.371	0.177		100.267
BU 21	1	56.137	0.077	3.501	0.962	4.255	0.104	0.102	34.860	0.576	0.135	0.005	100.714
BU 21	2	56.432	0.062	2.612	0.973	4.631	0.145	0.093	34.441	0.738	0.139	0.003	100.269
BU 25	3	58.372	0.112	1.189	0.766	4.600	0.106	0.088	35.666	0.635	0.136	0.065	101.735
BU 25	1	56.875	0.111	2.503	0.907	4.660	0.105	0.112	34.852	0.885	0.173	0.015	101.198
BU 25	2	58.185	0.004	0.644	0.332	4.387	0.103	0.194	36.301	0.389	0.096	0.001	100.636
BU 29	1	58.306	0.045	0.780	0.507	4.638	0.101	0.106	35.929	0.447	0.168	0.011	101.038
BU 29	4	58.939	0.042	1.107	0.717	4.786	0.121	0.099	35.880	0.518	0.194	0.003	102.406
BU 33	3	59.093	0.014	0.728	0.416	4.411	0.104	0.104	36.296	0.493	0.090	0.010	101.759
BU 33	4	58.633		0.598	0.385	4.205	0.098	0.111	36.173	0.444	0.137		100.784
BU 34	1	57.867	0.050	0.674	0.241	5.800	0.121	0.085	35.089	0.281	0.060	0.015	100.283

Table 7: Compositions of Olivine at Core

Sample	Garnet	SiO_2	TiO_2	Cr_2O_3	FeO	MnO	NiO	MgO	CaO	Total
BU 3	2	41.622	0.001	0.019	6.665	0.078	0.393	51.913	0.029	100.720
BU 3	3	41.464		0.024	6.663	0.078	0.436	52.170	0.018	100.853
BU 3	4	41.712	0.002	0.024	6.774	0.079	0.422	52.249	0.017	101.279
BU 3	1	41.769	0.003	0.019	6.790	0.086	0.395	52.427	0.012	101.501
BU 5	2	41.637		0.025	6.521	0.079	0.425	52.317	0.013	101.017
BU 6	2	42.095	0.003	0.029	7.387	0.072	0.411	51.512	0.033	101.542
BU 6	3	41.571	0.001	0.018	7.471	0.093	0.413	51.793	0.023	101.383
BU 13	3	41.556	0.002	0.021	7.289	0.083	0.400	52.106	0.020	101.477
BU 13	2	41.677		0.015	7.217	0.088	0.389	51.972	0.018	101.376
BU 13	1	41.510	0.007	0.011	7.274	0.088	0.388	51.803	0.016	101.097
BU 18	1	41.886		0.016	7.113	0.081	0.415	52.568	0.021	102.100
BU 18	2	41.826		0.007	7.162	0.090	0.418	52.669	0.025	102.197
BU 18	4	41.943		0.015	7.072	0.087	0.408	52.464	0.022	102.011
BU 18	5	41.767		0.010	7.052	0.079	0.412	52.494	0.016	101.830
BU 18	6	42.067		0.020	7.148	0.082	0.427	52.501	0.015	102.260
BU 21	3	42.027		0.045	6.580	0.087	0.420	52.423	0.010	101.592
BU 21	1	41.974		0.021	6.612	0.080	0.403	52.494	0.010	101.594
BU 21	2	41.905		0.019	6.555	0.082	0.410	52.230	0.011	101.212
BU 25	3	41.753		0.020	6.945	0.083	0.402	52.289	0.014	101.506
BU 25	1	41.849		0.025	6.942	0.081	0.400	52.416	0.015	101.728
BU 29	1	41.732	0.001	0.025	7.319	0.091	0.402	51.670	0.014	101.254
BU 29	2	41.957	0.008	0.028	7.367	0.091	0.408	52.323	0.018	102.200

Table 7: Olivine, Core (Continued)

Sample	Garnet	SiO_2	TiO_2	Cr_2O_3	FeO	MnO	NiO	MgO	CaO	Total
BU 29	3	41.607	0.002	0.030	7.314	0.106	0.384	52.145	0.017	101.605
BU 29	4	41.687	0.001	0.012	7.299	0.103	0.393	52.136	0.016	101.647
BU 33	1	41.805		0.013	6.847	0.095	0.393	52.563	0.021	101.737
BU 33	2	41.825		0.022	6.821	0.094	0.401	52.395	0.019	101.577
BU 33	3	41.688		0.031	6.783	0.094	0.384	52.275	0.020	101.275
BU 33	4	41.626		0.011	6.768	0.090	0.392	52.329	0.018	101.234
BU 34	1	41.359	0.013	0.007	9.140	0.117	0.383	50.564	0.012	101.595

Table 8: Compositions of Olivine at Rim

Sample	Garnet	SiO_2	TiO_2	Al_2O_3	Cr_2O_3	FeO	MnO	NiO	MgO	CaO	Total
BU 3	3	41.467	0.001		0.078	6.684	0.096	0.391	52.285	0.043	101.045
BU 3	4	42.277	0.003		0.045	6.736	0.093	0.407	52.947	0.026	102.534
BU 3	1	41.268			0.060	6.967	0.091	0.390	51.764	0.027	100.567
BU 5	2	41.282	0.009		0.112	6.847	0.106	0.385	51.976	0.032	100.749
BU 6	3	40.487			0.025	7.315	0.085	0.401	51.182	0.020	99.515
BU 13	2	40.505	0.009		0.04	7.312	0.102	0.366	50.903	0.048	99.285
BU 13	1	42.052	0.006		0.046	7.433	0.117	0.327	51.764	0.070	101.815
BU 18	1	42.259			0.070	7.092	0.089	0.407	52.325	0.043	102.285
BU 18	2	42.122	0.002		0.042	6.939	0.102	0.426	52.646	0.036	102.315
BU 18	4	42.121			0.032	7.128	0.080	0.406	52.062	0.040	101.869
BU 18	5	42.072	0.001		0.067	7.113	0.096	0.414	52.630	0.042	102.435

Table 8: Olivine, Rim (Continued)

Sample	Garnet	SiO_2	TiO_2	Al_2O_3	Cr_2O_3	FeO	MnO	NiO	MgO	CaO	Total
BU 18	6	41.899	0.005		0.069	7.006	0.083	0.409	52.171	0.031	101.673
BU 21	3	41.810			0.030	6.423	0.087	0.402	53.252	0.022	102.026
BU 21	1	41.571			0.042	6.947	0.116	0.394	51.531	0.027	100.628
BU 25	3	41.901	0.004		0.043	7.635	0.117	0.372	51.205	0.078	101.355
BU 25	1	41.636			0.054	7.600	0.140	0.382	51.679	0.027	101.518
BU 29	1	41.345	0.012		0.061	7.195	0.097	0.379	51.763	0.023	100.875
BU 29	2	41.400	0.008		0.050	7.243	0.094	0.379	51.988	0.017	101.179
BU 29	3	42.225	0.011		0.048	7.368	0.111	0.372	52.481	0.034	102.650
BU 29	4	42.566	0.019	0.499	0.048	6.842	0.097	0.366	50.423	0.032	100.892
BU 33	2	42.108			0.045	6.837	0.086	0.381	52.68	0.029	102.166
BU 33	3	41.636	0.003		0.061	6.911	0.094	0.382	52.946	0.031	102.064
BU 33	4	42.953			0.007	6.813	0.072	0.392	52.607	0.023	102.867
BU 34	1	41.374	0.016		0.037	10.096	0.126	0.352	50.004	0.036	102.041

Table 9: BU 6 Transect CPX-GRT

Clinopyroxene

Location	Distance	SiO_2	TiO_2	Al_2O_3	Cr_2O_3	FeO	MnO	NiO	MgO	CaO	Na_2O	K_2O	Total
Core	0.0E+00	54.933	0.019	1.752	1.373	2.081	0.078	0.042	17.329	20.922	1.527	0.006	100.062
	5.0E-05	54.661	0.018	1.728	1.366	2.100	0.058	0.040	17.179	21.132	1.519	0.010	99.811
	1.0E-04	56.247	0.023	1.723	1.435	2.085	0.059	0.062	17.161	20.752	1.556	0.013	101.116
	1.5E-04	55.052	0.017	1.702	1.348	2.081	0.079	0.068	17.164	21.132	1.524	0.009	100.176
	2.0E-04	55.558	0.019	1.729	1.418	2.111	0.060	0.047	17.152	21.013	1.527	0.008	100.642
	2.5E-04	55.688	0.013	1.733	1.386	2.101	0.061	0.066	17.122	21.138	1.514	0.004	100.826
	3.0E-04	55.315	0.017	1.732	1.451	2.081	0.079	0.060	17.211	21.104	1.542	0.005	100.597
	3.5E-04	55.240	0.022	1.720	1.403	2.141	0.071	0.054	17.204	21.161	1.513	0.008	100.537
	4.0E-04	55.367	0.023	1.731	1.425	2.120	0.033	0.057	17.198	21.117	1.502	0.009	100.582
	4.5E-04	55.239	0.014	1.770	1.376	2.061	0.081	0.048	17.218	21.088	1.515	0.010	100.420
	5.0E-04	55.577	0.023	1.755	1.449	2.153	0.081	0.052	17.180	20.956	1.505	0.004	100.735
	5.5E-04	56.646	0.023	1.786	1.409	2.111	0.032	0.049	17.162	20.695	1.526	0.011	101.450
	6.0E-04	56.019	0.031	1.755	1.395	2.102	0.068	0.057	17.235	20.814	1.546	0.006	101.028
	6.5E-04	55.008	0.049	1.918	1.413	2.199	0.064	0.055	17.454	21.051	1.379		100.590
	7.0E-04	53.727	0.215	2.060	1.065	2.402	0.137	0.040	17.699	22.680	0.623		100.648
	7.5E-04	56.262	0.026	1.908	1.363	2.208	0.090	0.054	17.305	20.219	1.498	0.011	100.944
	8.0E-04	55.464	0.025	1.870	1.412	2.176	0.074	0.047	17.269	21.109	1.484	0.008	100.938
	8.5E-04	55.417	0.031	2.042	1.453	2.195	0.044	0.071	17.394	20.799	1.584	0.001	101.031
Rim	9.0E-04	55.423	0.038	2.634	1.590	2.282	0.063	0.046	16.935	20.825	1.669	0.051	101.556

Table 9: BU 6 Transect CPX-GRT (Continued)

Garnet												
Location	Distance	SiO_2	TiO_2	Al_2O_3	Cr_2O_3	FeO	MnO	NiO	MgO	CaO	Na_2O	Total
Rim	4.0E-04	42.582	0.046	21.020	4.303	6.678	0.351		21.117	5.401	0.008	101.506
↑	3.5E-04	42.317	0.045	20.922	4.299	6.820	0.353	0.007	20.925	5.321	0.024	101.033
	3.0E-04	42.368	0.031	21.012	4.270	6.853	0.344	0.001	20.816	5.321	0.022	101.038
	2.5E-04	42.186	0.033	20.923	4.268	6.808	0.343	0.003	20.695	5.348	0.001	100.608
	2.0E-04	42.538	0.036	21.045	4.316	6.887	0.360		20.970	5.356	0.029	101.537
	1.5E-04	42.190	0.039	20.799	4.296	6.874	0.348	0.008	20.848	5.351	0.026	100.779
	1.0E-04	42.223	0.042	20.775	4.325	6.813	0.351	0.008	20.813	5.351		100.701
	5.0E-05	42.195	0.049	20.838	4.316	6.822	0.359	0.009	20.809	5.355	0.022	100.774
Core	0.0E+00	42.416	0.037	21.035	4.382	6.940	0.345	0.007	20.876	5.408	0.036	101.482

Table 10: BU 21 Transect OL-GRT-OPX

Olivine

Location	Distance	SiO_2	TiO_2	Al_2O_3	Cr_2O_3	FeO	MnO	NiO	MgO	CaO	Total
Core	0.0E+00	41.851		0.011	0.033	6.626	0.080	0.428	52.877	0.009	101.915
	5.0E-05	41.773		0.001	0.013	6.544	0.075	0.406	52.747	0.008	101.567
	1.0E-04	41.800			0.025	6.578	0.076	0.426	52.734	0.012	101.651
	1.5E-04	41.624			0.015	6.593	0.080	0.401	52.724	0.009	101.446
	2.0E-04	41.896	0.002	0.007	0.014	6.599	0.078	0.417	52.901	0.008	101.922
	2.5E-04	41.857			0.033	6.617	0.069	0.408	52.856	0.008	101.848
	3.0E-04	41.888			0.020	6.499	0.062	0.413	52.547	0.014	101.443
	3.5E-04	41.870			0.021	6.544	0.087	0.414	52.376	0.011	101.323
	4.0E-04	41.955			0.025	6.612	0.090	0.399	52.619	0.011	101.711
	4.5E-04	41.860	0.012	0.004	0.009	6.694	0.084	0.394	52.716	0.089	101.862
	5.0E-04	41.894		0.005	0.015	6.550	0.084	0.403	52.532	0.011	101.494
	5.5E-04	41.892	0.004	0.006	0.022	6.511	0.073	0.398	52.436	0.049	101.391
	6.0E-04	41.753			0.021	6.485	0.086	0.416	52.193	0.008	100.962
	6.5E-04	41.910			0.033	6.459	0.079	0.405	52.361	0.011	101.258
	7.0E-04	41.936		0.009	0.041	6.587	0.091	0.405	52.715	0.015	101.799
Rim	7.5E-04	41.997	0.009	0.019	0.050	6.859	0.105	0.394	51.928	0.031	101.392

Table 10: BU 21 Transect OL-GRT-OPX (Continued)

Garnet-Segment 1

Location	Distance	SiO_2	TiO_2	Al_2O_3	Cr_2O_3	FeO	MnO	NiO	MgO	CaO	Na_2O	Total
Rim	7.5E-04	42.014	0.016	20.662	4.719	6.416	0.308	0.017	21.748	4.594	0.053	100.547
	7.0E-04	41.854	0.011	20.301	5.047	6.509	0.331	0.009	21.586	4.781	0.029	100.458
	6.5E-04	42.491	0.117	22.042	2.954	6.386	0.404	0.009	21.946	4.413	0.020	100.782
	6.0E-04	42.297	0.010	20.325	5.322	6.423	0.310		21.194	5.181	0.033	101.095
	5.5E-04	42.342	0.012	20.320	5.212	6.300	0.311	0.014	21.206	5.205	0.029	100.951
	5.0E-04	42.207	0.009	20.373	5.005	6.331	0.311		21.192	5.088	0.015	100.531
	4.5E-04	42.434	0.007	20.390	5.109	6.319	0.330	0.006	21.262	5.073	0.028	100.958
	4.0E-04	42.195	0.009	20.356	5.037	6.371	0.326	0.002	21.044	5.132	0.022	100.494
	3.5E-04	42.049	0.005	20.422	4.957	6.308	0.332		21.257	5.081	0.027	100.438
	3.0E-04	42.326	0.006	20.517	4.840	6.294	0.314		21.227	5.056	0.029	100.609
	2.5E-04	42.321	0.001	20.696	4.800	6.287	0.319	0.007	21.403	4.985	0.031	100.850
	2.0E-04	42.544	0.005	20.792	4.805	6.374	0.315		21.354	4.929	0.035	101.153
	1.5E-04	42.406	0.007	20.760	4.665	6.385	0.307	0.011	21.380	5.004	0.038	100.963
	1.0E-04	42.508	0.004	20.929	4.531	6.300	0.326	0.006	21.418	4.844	0.020	100.886
Halfway to	5.0E-05	42.371	0.003	20.799	4.628	6.368	0.315	0.006	21.299	4.816	0.024	100.629
Core	0.0E+00	42.279	0.003	20.846	4.542	6.309	0.315		21.251	4.950	0.029	100.524

Table 10: BU 21 Transect OL-GRT-OPX (Continued)

Garnet-Segment 2

Location	Distance	SiO_2	TiO_2	Al_2O_3	Cr_2O_3	FeO	MnO	NiO	MgO	CaO	Na_2O	Total
Halfway to	6.0E-04	42.470	0.002	20.995	4.352	6.267	0.310	0.014	21.398	4.908	0.026	100.742
Core	5.0E-04	42.424	0.003	21.025	4.375	6.352	0.323	0.010	21.414	4.916	0.017	100.859
↑	4.0E-04	42.267		20.986	4.371	6.311	0.324		21.343	4.880	0.027	100.509
	3.0E-04	42.572		21.092	4.344	6.294	0.316	0.005	21.469	4.907	0.038	101.037
	2.0E-04	42.360		20.984	4.319	6.320	0.334		21.466	4.854	0.031	100.668
	1.0E-04	42.536		21.191	4.308	6.369	0.319		21.411	4.892	0.040	101.066
Core	0.0E+00	42.418		20.980	4.346	6.318	0.323	0.004	21.322	5.006	0.027	100.744

Garnet-Segment 3

Location	Distance	SiO_2	TiO_2	Al_2O_3	Cr_2O_3	FeO	MnO	NiO	MgO	CaO	Na_2O	Total
Core	0.0E+00	42.574		21.092	4.356	6.390	0.328	0.013	21.540	4.813	0.033	101.139
↓	1.0E-04	42.581	0.002	21.047	4.338	6.294	0.309	0.002	21.373	4.902	0.016	100.864
	2.0E-04	42.288		20.995	4.363	6.364	0.313	0.014	21.307	4.902	0.019	100.565
	3.0E-04	42.776	0.005	21.159	4.342	6.367	0.318	0.015	21.528	4.881	0.028	101.419
	4.0E-04	42.393		21.036	4.325	6.291	0.307	0.000	21.342	4.865	0.015	100.574
	5.0E-04	42.913	0.001	21.236	4.334	6.298	0.313	0.007	21.492	4.999	0.033	101.626
	6.0E-04	42.621		20.986	4.467	6.365	0.321	0.002	21.382	4.924	0.038	101.106
	7.0E-04	42.518		20.960	4.439	6.273	0.314	0.001	21.387	4.927	0.041	100.860

Table 10: BU 21 Transect OL-GRT-OPX (Continued)

Location	Distance	SiO_2	TiO_2	Al_2O_3	Cr_2O_3	FeO	MnO	NiO	MgO	CaO	Na_2O	Total
↓	8.0E-04	42.458	0.002	20.991	4.487	6.331	0.307	0.001	21.309	4.887	0.040	100.813
	9.0E-04	42.353	0.004	20.874	4.589	6.311	0.318	0.011	21.352	4.920	0.023	100.755
Halfway to	1.0E-03	42.324	0.003	20.872	4.603	6.318	0.321	0.003	21.384	4.880	0.028	100.736
Rim	1.1E-03	42.287	0.002	20.806	4.617	6.373	0.316	0.000	21.348	4.953	0.032	100.734

Table 10: BU 21 Transect OL-GRT-OPX (Continued)

Garnet-Segment 4

Location	Distance	SiO_2	TiO_2	Al_2O_3	Cr_2O_3	FeO	MnO	NiO	MgO	CaO	Na_2O	Total
Halfway to	0.0E+00	42.444		20.783	4.723	6.245	0.326	0.001	21.238	5.005	0.032	100.797
Rim	5.0E-05	42.390		20.706	4.730	6.278	0.311		21.199	5.023	0.020	100.657
↓	1.0E-04	42.419	0.004	20.642	4.808	6.277	0.318		21.203	5.063	0.034	100.768
	1.5E-04	42.290	0.003	20.599	4.873	6.299	0.322	0.007	21.067	5.061	0.024	100.545
	2.0E-04	42.089	0.002	20.511	4.900	6.311	0.324		21.040	4.956	0.033	100.166
	2.5E-04	40.754	0.026	19.619	4.933	6.071	0.322	0.002	20.398	5.129	0.028	97.282
	3.0E-04	42.470	0.001	20.655	4.826	6.317	0.317		21.310	5.169	0.022	101.087
	3.5E-04	42.391	0.005	20.570	4.965	6.297	0.322		21.072	5.115	0.031	100.768
	4.0E-04	42.194	0.003	20.431	5.066	6.283	0.314	0.005	20.978	5.152	0.015	100.441
	4.5E-04	42.550	0.131	21.984	3.068	6.255	0.384		21.758	4.423	0.025	100.578
	5.0E-04	42.568	0.138	21.906	3.263	5.864	0.358	0.005	22.192	4.417	0.026	100.737
Rim	5.5E-04	42.171	0.014	20.297	5.059	6.354	0.299	0.008	21.336	4.840	0.025	100.403

Table 10: BU 21 Transect OL-GRT-OPX (Continued)

Orthopyroxene

Location	Distance	SiO_2	TiO_2	Al_2O_3	Cr_2O_3	FeO	MnO	NiO	MgO	CaO	Na_2O	K_2O	Total
Rim	7.5E-04	56.063	0.076	3.829	0.929	4.571	0.137	0.099	34.797	0.610	0.127	0.007	101.245
	7.0E-04	58.462		0.837	0.395	4.090	0.081	0.113	36.395	0.349	0.199		100.921
↑	6.5E-04	58.470		0.807	0.375	4.141	0.096	0.096	36.438	0.345	0.129		100.897
	6.0E-04	58.369		0.795	0.401	4.086	0.084	0.101	36.366	0.349	0.139		100.690
	5.5E-04	58.438		0.774	0.357	4.087	0.086	0.097	36.342	0.349	0.164		100.694
	5.0E-04	58.558		0.780	0.376	4.108	0.104	0.104	36.436	0.342	0.151		100.959
	4.5E-04	58.411	0.002	0.783	0.373	4.107	0.089	0.097	36.493	0.343	0.148		100.846
	4.0E-04	58.284		0.785	0.368	4.126	0.090	0.094	36.466	0.340	0.153	0.002	100.708
	3.5E-04	58.423	0.001	0.797	0.369	4.147	0.100	0.097	36.438	0.337	0.168	0.002	100.879
	3.0E-04	58.430	0.001	0.792	0.375	4.093	0.093	0.093	36.421	0.344	0.164		100.806
	2.5E-04	58.461		0.789	0.372	4.111	0.096	0.099	36.397	0.334	0.135		100.794
	2.0E-04	58.359		0.801	0.370	4.055	0.088	0.101	36.222	0.347	0.179	0.003	100.525
	1.5E-04	58.386		0.789	0.359	4.113	0.097	0.104	36.423	0.338	0.163		100.772
	1.0E-04	58.238		0.765	0.355	4.071	0.080	0.099	36.332	0.342	0.156	0.002	100.440
	5.0E-05	58.316		0.762	0.372	4.155	0.085	0.092	36.379	0.342	0.146		100.649
Core	0.0E+00	58.200		0.772	0.352	4.048	0.086	0.086	36.324	0.348	0.165		100.381

Table 11: BU 29 Transect OL-GRT-OL

Olivine 1

Location	Distance	SiO_2	TiO_2	Al_2O_3	Cr_2O_3	FeO	MnO	NiO	MgO	CaO	Total
Core	0.0E+00	41.696	0.006	0.010	0.035	7.327	0.088	0.397	51.660	0.009	101.228
	5.0E-05	41.415	0.006		0.037	7.296	0.091	0.392	51.960	0.014	101.211
	1.0E-04	42.078	0.009	0.007	0.031	7.213	0.102	0.381	51.690	0.016	101.527
	1.5E-04	42.386	0.005	0.005	0.027	7.255	0.095	0.384	51.987	0.014	102.158
	2.0E-04	42.088	0.010		0.030	7.239	0.092	0.373	51.369	0.013	101.214
	2.5E-04	40.805	0.008	0.003	0.020	7.230	0.083	0.380	51.767	0.009	100.305
	3.0E-04	41.320	0.013	0.002	0.018	7.248	0.099	0.398	51.345	0.013	100.456
	3.5E-04	41.279	0.008		0.031	7.206	0.095	0.406	51.089	0.011	100.125
	4.0E-04	40.798	0.002	0.008	0.024	7.225	0.094	0.400	50.843	0.013	99.407
	4.5E-04	40.630	0.009	0.005	0.023	7.269	0.094	0.392	51.048	0.013	99.483
	5.0E-04	41.119	0.009	0.005	0.014	7.251	0.077	0.396	50.690	0.013	99.574
	5.5E-04	41.820	0.004	0.004	0.016	7.169	0.107	0.392	52.784	0.012	102.308
	6.0E-04	41.665	0.013	0.005	0.033	7.239	0.098	0.382	52.492	0.013	101.940
	6.5E-04	41.502	0.003	0.003	0.038	7.106	0.085	0.410	51.752	0.082	100.981
	7.0E-04	41.048	0.007	0.007	0.042	7.325	0.102	0.388	52.189	0.016	101.124
Rim	7.5E-04	41.483	0.006	0.011	0.114	7.463	0.105	0.368	51.243	0.030	100.823

Table 11: BU 29 Transect OL-GRT-OL (Continued)

Garnet-Segment 1

Location	Distance	SiO_2	TiO_2	Al_2O_3	Cr_2O_3	FeO	MnO	NiO	MgO	CaO	Na_2O	Total
Core	0.0E+00	41.830	0.156	21.414	3.166	6.666	0.373	0.023	21.627	4.412	0.026	99.693
↓	5.0E-05	41.799	0.149	19.703	5.296	6.832	0.373	0.019	21.090	4.933	0.043	100.237
	1.0E-04	41.965	0.178	21.423	3.345	6.475	0.397		21.087	5.288	0.023	100.181
	1.5E-04	41.731	0.139	20.026	5.096	6.843	0.342		21.076	4.912	0.058	100.223
	2.0E-04	41.679	0.152	19.693	5.417	6.736	0.362	0.004	20.849	4.995	0.050	99.937
	2.5E-04	41.513	0.144	19.522	5.499	6.704	0.333	0.019	20.571	5.357	0.051	99.713
	3.0E-04	41.602	0.144	19.590	5.494	6.763	0.350	0.009	20.683	5.273	0.051	99.959
	3.5E-04	41.615	0.146	19.584	5.557	6.718	0.347	0.006	20.548	5.366	0.048	99.935
	4.0E-04	41.724	0.148	19.572	5.552	6.725	0.359	0.001	20.643	5.289	0.043	100.056
	4.5E-04	41.746	0.150	19.641	5.544	6.792	0.352		20.665	5.211	0.045	100.146
	5.0E-04	41.717	0.148	19.552	5.524	6.790	0.358		20.673	5.194	0.061	100.017
Rim	5.5E-04	41.598	0.151	19.538	5.532	6.813	0.335		20.657	5.160	0.045	99.829

Table 11: BU 29 Transect OL-GRT-OL (Continued)

Garnet-Segment 2

Location	Distance	SiO_2	TiO_2	Al_2O_3	Cr_2O_3	FeO	MnO	NiO	MgO	CaO	Na_2O	Total
Top Core	0.0E+00	41.598	0.155	19.484	5.602	6.753	0.337	0.004	20.567	5.327	0.050	99.877
↕	5.0E-05	41.638	0.149	19.551	5.579	6.776	0.346	0.002	20.791	5.206	0.054	100.092
	1.0E-04	41.825	0.151	19.605	5.552	6.792	0.355		20.764	5.210	0.054	100.308
	1.5E-04	41.817	0.147	19.595	5.596	6.768	0.340		20.653	5.251	0.071	100.238
	2.0E-04	41.794	0.155	19.512	5.543	6.735	0.353	0.016	20.598	5.167	0.041	99.914
Bottom Core	2.5E-04	41.786	0.151	19.480	5.512	6.807	0.363	0.007	20.754	5.211	0.045	100.116

Garnet-Segment 3

Location	Distance	SiO_2	TiO_2	Al_2O_3	Cr_2O_3	FeO	MnO	NiO	MgO	CaO	Na_2O	Total
Core	0.0E+00	41.681	0.148	19.530	5.526	6.802	0.359	0.011	20.663	5.144	0.036	99.900
↓	5.0E-05	41.814	0.145	19.530	5.555	6.848	0.355	0.000	20.787	5.179	0.045	100.258
	1.0E-04	41.563	0.156	19.494	5.451	6.824	0.357	0.007	20.613	5.098	0.061	99.624
	1.5E-04	41.710	0.150	19.580	5.493	6.758	0.362	0.001	20.718	5.082	0.039	99.893
	2.0E-04	41.616	0.155	19.579	5.452	6.732	0.348	0.001	20.795	5.045	0.033	99.756
	2.5E-04	41.661	0.151	19.578	5.520	6.793	0.360	0.017	20.815	5.075	0.039	100.009
	3.0E-04	41.778	0.152	19.678	5.490	6.765	0.356	0.016	20.713	5.103	0.058	100.109
	3.5E-04	41.714	0.146	19.575	5.444	6.833	0.335	0.013	20.742	5.107	0.052	99.961
	4.0E-04	41.811	0.149	19.599	5.492	6.794	0.367	0.008	20.696	5.070	0.047	100.033
	4.5E-04	41.675	0.150	19.597	5.443	6.764	0.365	0.011	20.652	5.056	0.034	99.747
	5.0E-04	41.927	0.159	21.163	3.821	6.370	0.374	0.002	21.617	4.384	0.021	99.838
Rim	5.5E-04	41.781	0.152	21.265	3.536	6.392	0.365	0.010	21.212	4.640	0.027	99.380

Table 11: BU 29 Transect OL-GRT-OL (Continued)

Olivine 2

Location	Distance	SiO_2	TiO_2	Al_2O_3	Cr_2O_3	FeO	MnO	NiO	MgO	CaO	Total
Core	0.0E+00	40.709	0.008	0.013	0.058	7.264	0.087	0.386	51.514	0.023	100.062
	5.0E-05	40.604	0.006	0.010	0.027	7.272	0.102	0.401	51.612	0.015	100.049
↓	1.0E-04	39.930	0.004	0.004	0.042	7.298	0.096	0.410	51.335	0.017	99.136
	1.5E-04	39.958	0.009	0.008	0.027	7.239	0.079	0.394	51.126	0.017	98.857
	2.0E-04	39.909	0.008	0.002	0.028	7.310	0.091	0.381	51.135	0.015	98.879
	2.5E-04	40.050	0.013	0.002	0.026	7.262	0.094	0.390	51.281	0.010	99.128
	3.0E-04	40.406	0.007	0.015	0.030	7.317	0.094	0.407	51.747	0.018	100.041
	3.5E-04	40.683	0.003	0.004	0.028	7.333	0.093	0.399	51.644	0.014	100.201
	4.0E-04	40.819	0.008		0.022	7.264	0.085	0.386	51.692	0.014	100.290
	4.5E-04	40.891	0.004	0.006	0.020	7.277	0.082	0.395	51.684	0.015	100.374
Rim	5.0E-04	40.853	0.004	0.001	0.027	7.282	0.096	0.391	51.363	0.012	100.029

Thermobarometry Results: Core *Temperatures (°C) and Pressures (kbar)*

Sample	Garnet	T_{BKN}	T_1	T_2	P_{BKN}	T_{BKN}	T_1	T_2	P_{KB}	T_{Krogh}	T_1	T_2	P_{BKN}	$T_{O'Neill}$ & Wood	P_{BKN}	T_{NT}	P_{NT}
BU 3	2													990	40		
BU 6	1a	938	997		44					669	925		28			885	43
BU 6	1b															893	44
BU 6	2															887	45
BU 6	3	940	986	996	40	930	958	982	33	679	920	964	25	992	43	894	44
BU 13	3													982	44		
BU 13	1													1009	45		
BU 18	1													1010	45		
BU 18	2													1014	43		
BU 18	4													987	42		
BU 18	5													996	44		
BU 18	6	928	981	1033	39	940	1017	1050	48	651	913	1000	24	1019	45	893	45
BU 21	3	1064	941	1237	44	1155	1147	1357	92	899	901	1214	34	931	36		
BU 21	1	1047	953	1166	45	1127	1136	1267	87	983	937	1157	41	964	40		
BU 21	2	1238	992	1283	57	1378	1276	1450	124	928	913	1236	38	950	39		
BU 25	3													993	44		
BU 25	1	1159	1004	1252	53	1232	1163	1342	90	906	937	1214	37	970	41	1109	52
BU 29	1	1049	988	1328	44	1107	1122	1408	75	932	957	1310	37	980	40		
BU 29	4	1036	978	1032	43	1065	1050	1067	60	802	918	1003	30	965	39	916	43
BU 33	1	993	989	1027	42	997	1001	1032	44	701	919	993	26	978	41	920	43
BU 33	3	1124	1026	1083	52	1156	1101	1120	69	864	957	1049	36	998	44	1056	42
BU 33	4b													988	41		
BU 34	1	806	855	777	34	802	846	774	32	616	807	757	22	842	36	735	34

Thermobarometry Results: Rim *Temperatures (°C) and Pressures (kbar)*

Sample	Garnet	T_{BKN}	T_1	T_2	P_{BKN}	T_{BKN}	T_1	T_2	P_{KB}	T_{Krogh}	T_1	T_2	P_{BKN}	$T_{O'Neill}$ & Wood	P_{BKN}	T_{NT}	P_{NT}
BU 3	4													998.2	41.57		
BU 6	1a	960	45.6	1013						714.4	30.31	944.8				895.3	40.84
BU 6	1b															910.3	33.94
BU 6	2															988.7	43.07
BU 6	3	1048	45.76	1022	1061	1063	54.49	1062	1080	763.3	28.9	946.9	1024	1002	42.89	966.2	36.04
BU 13	1													1060	51.16		
BU 18	1													970.9	41.48		
BU 18	6					992.6	32.92	1012	1098							967.7	46.28
BU 21	3	1208	47.95	978.8	1304	1289	87.29	1148	1405	864.6	28.83	896.7	1256	837.9	27.46	1146	45.52
BU 21	2															1109	50.65
BU 25	3													1125	46.47		
BU 25	1					1164	59.32	1241	1343							1071	42.02
BU 29	1													950.9	37		
BU 29	4					1016	35.23	988.9	1295							971.6	41.09
BU 33	1															971.6	42.21
BU 33	3	1220	56.06	1073	1187	1250	71.09	1140	1222	868.2	34.84	977.3	1137	980	41.26	1225	72.34
BU 33	4b													987	42.14		
BU 34	1					1021	28.04	843.7	778.4							909.9	33.75

Images

Traverse Image BU 6: Cpx, Segment 1; Garnet Segment 1

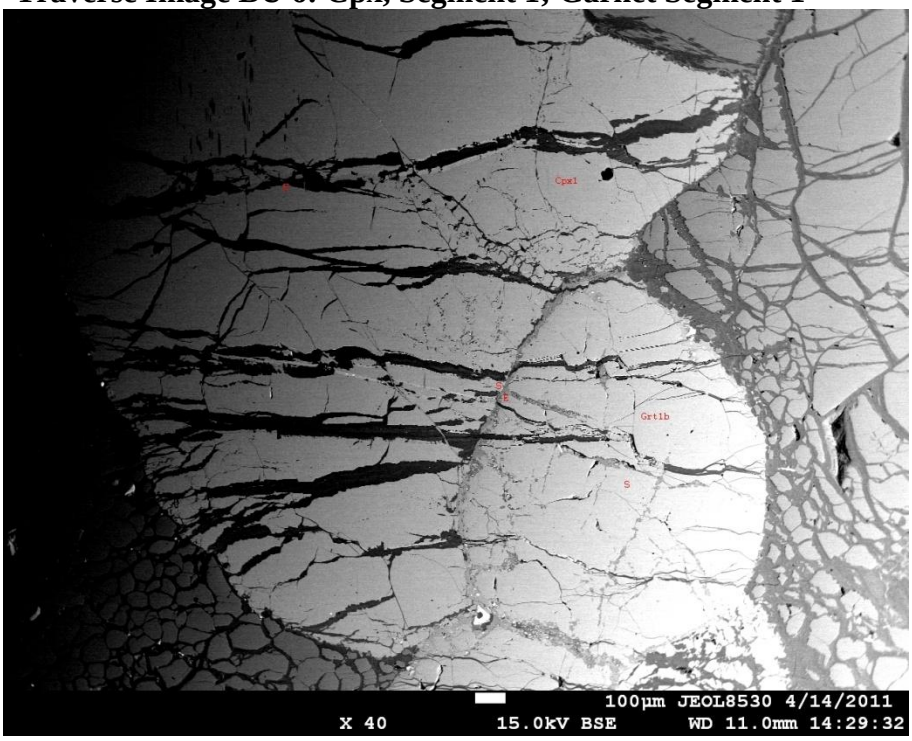

Traverse Locations BU 6: Cpx

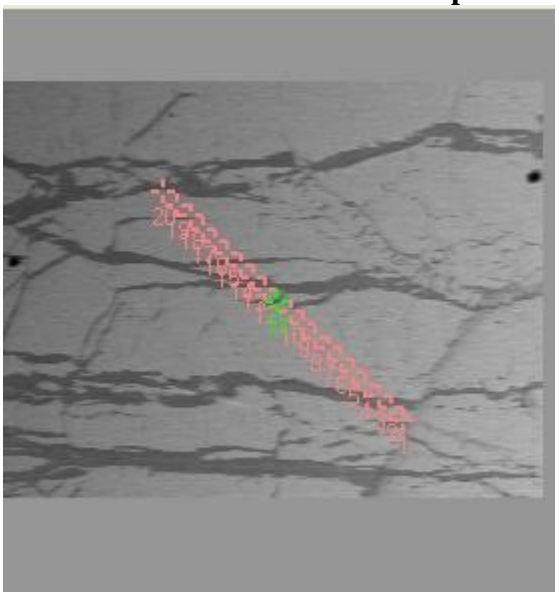

Traverse Locations BU 6: Garnet

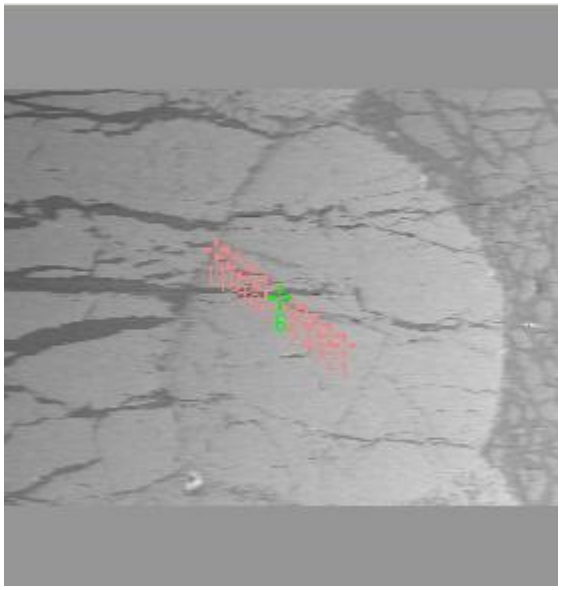

Traverse Image BU 21: Olivine, Segment 1; Garnet Segments 1 & 2

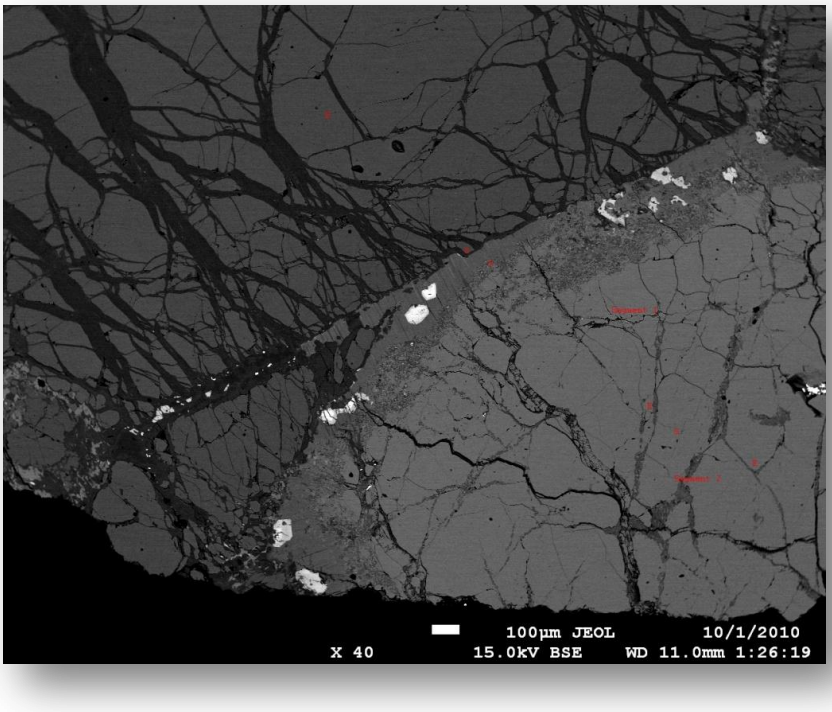

BU 21: Garnet Segments 3 & 4; Orthopyroxene Segment 1

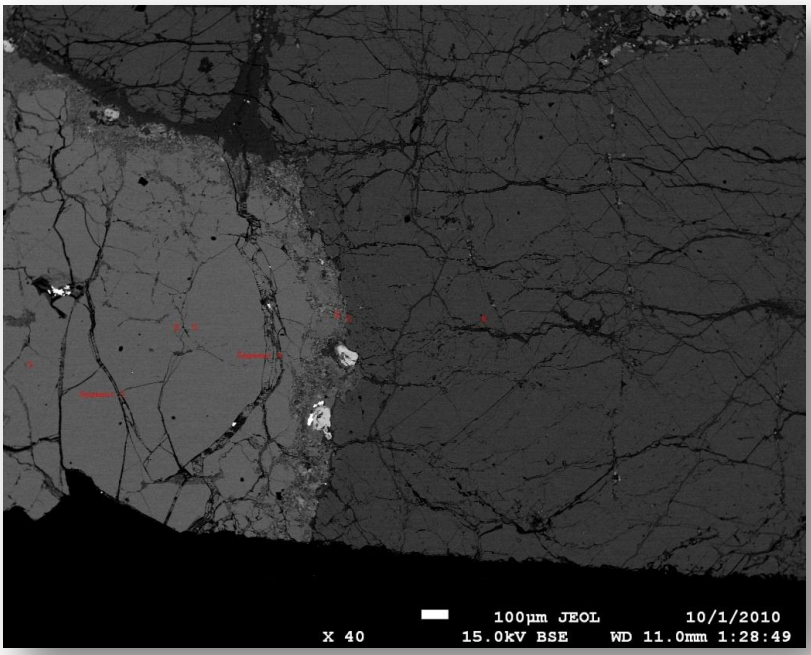

Traverse Image BU 29: Olivine Segment 1a

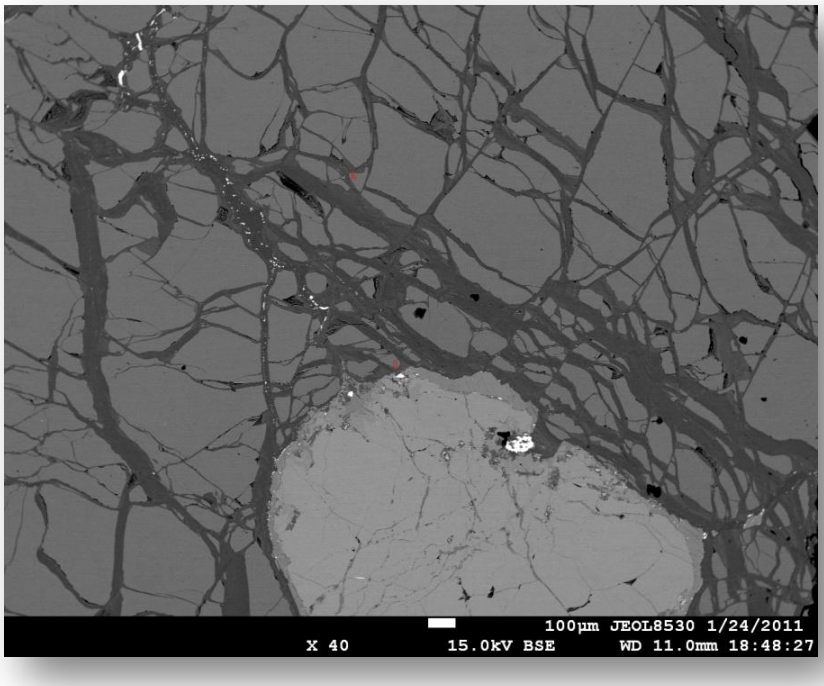

BU 29: Olivine Segment 1b

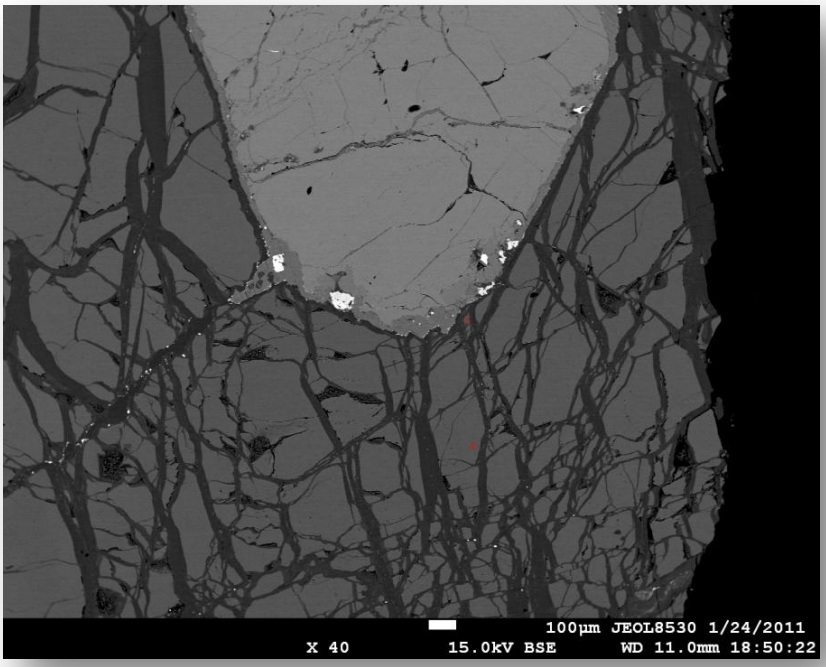

BU 29: Garnet Segments 1, 2, &3

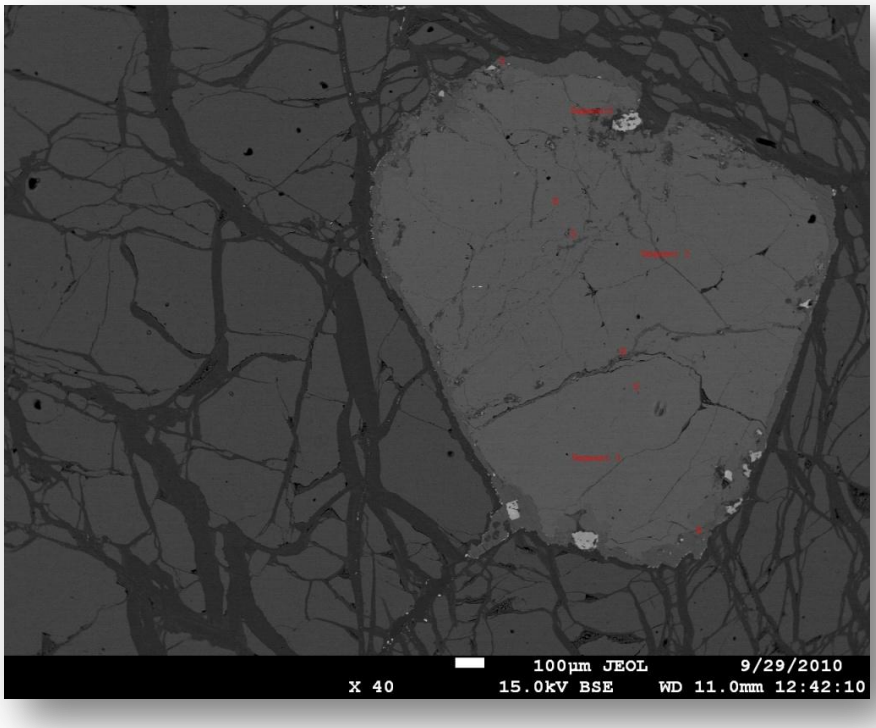

Compositional Maps

BU 21: Aluminum

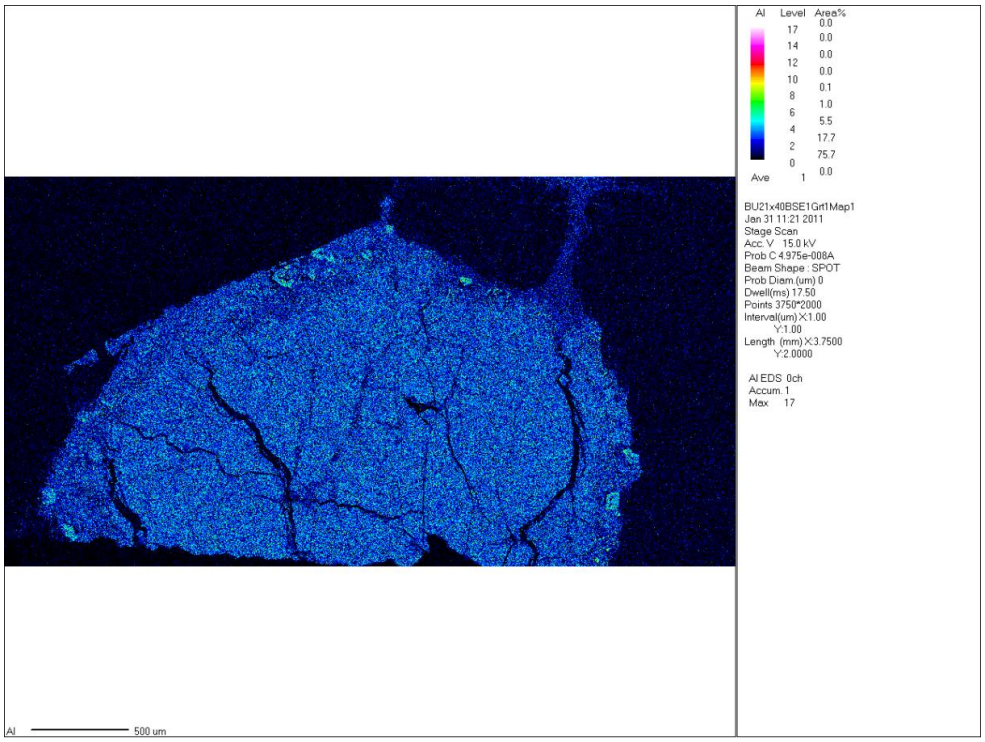

BU 21: Calcium

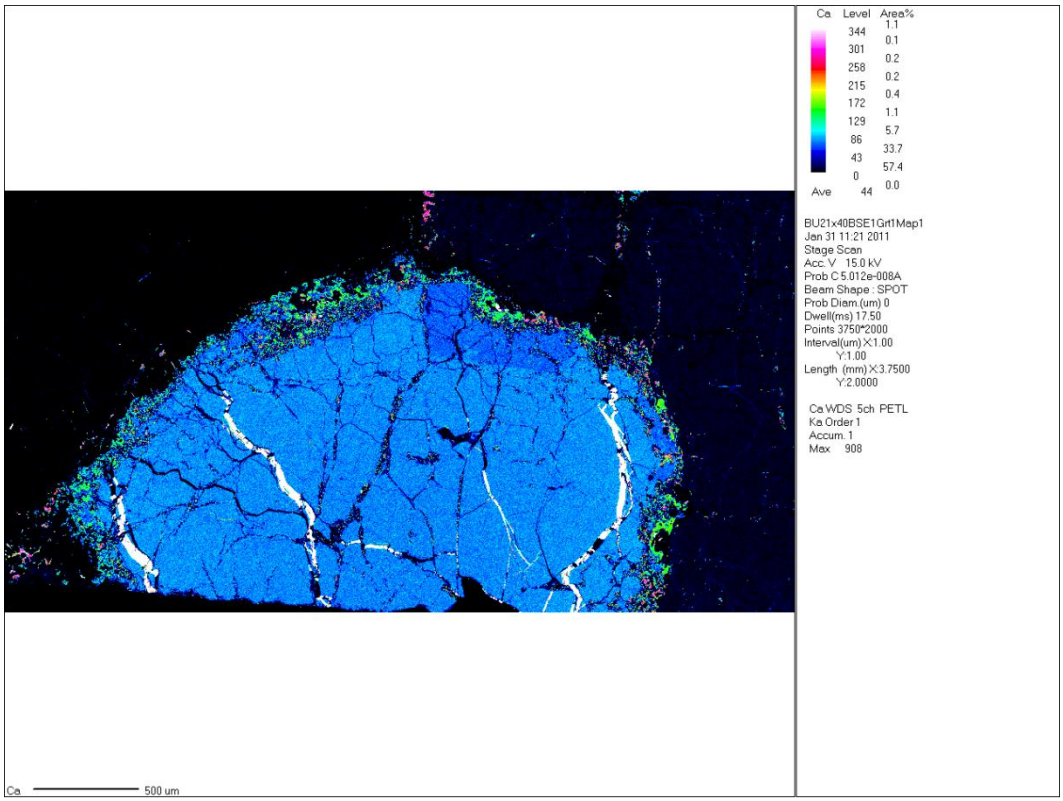

BU 21: Chromium

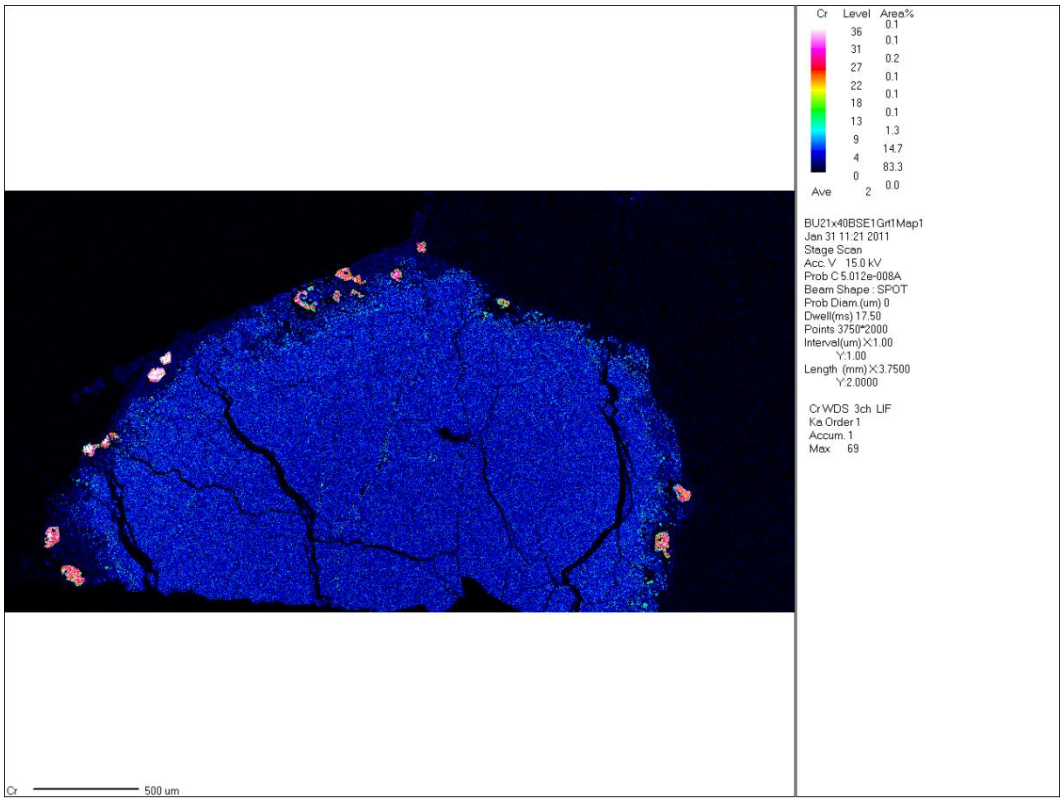

BU 21: Iron

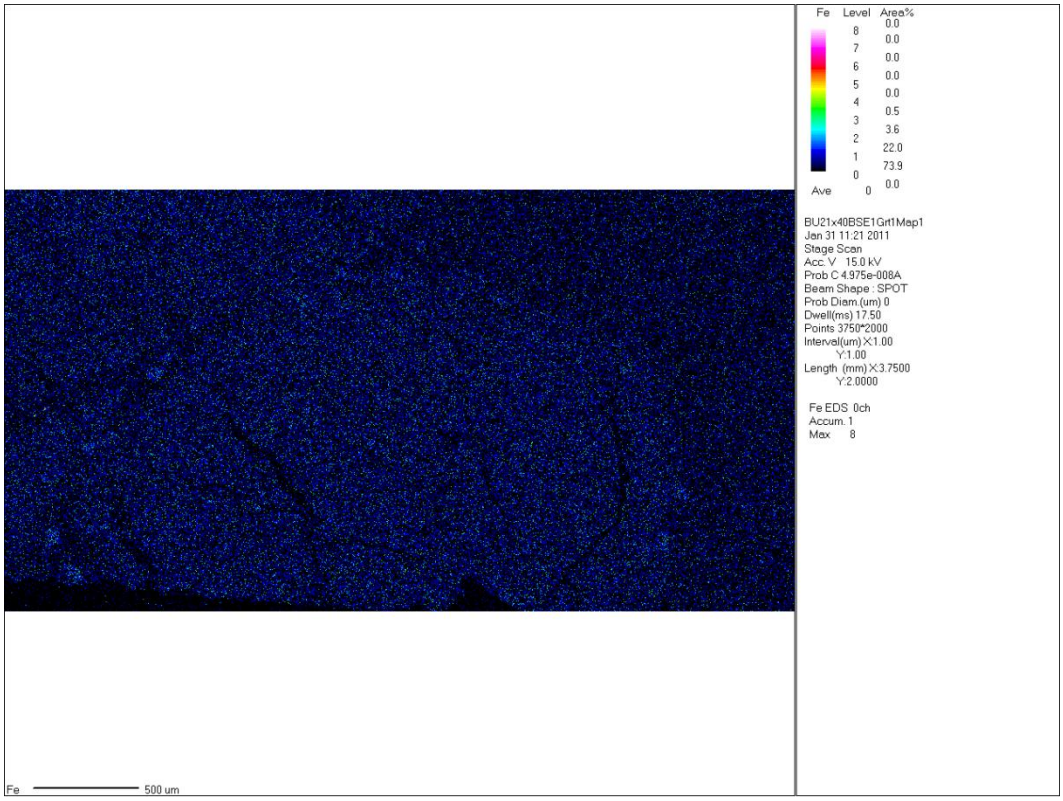

BU 21: Magnesium

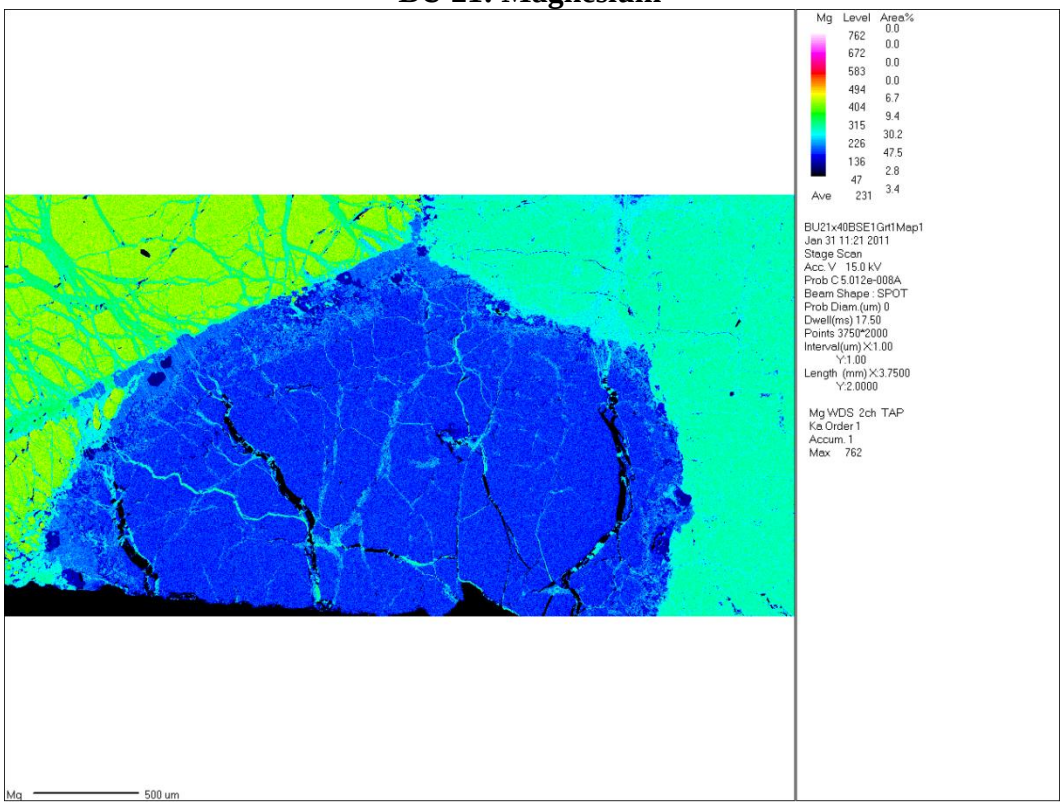

BU 29: Aluminum

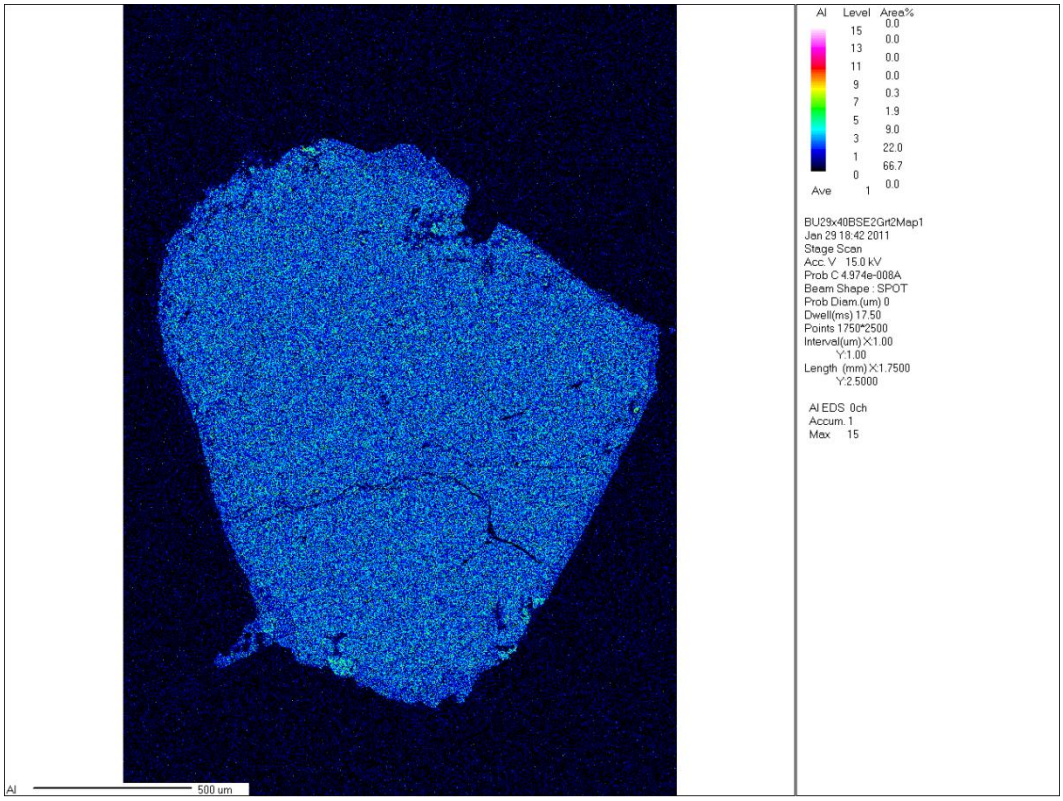

BU 29: Calcium

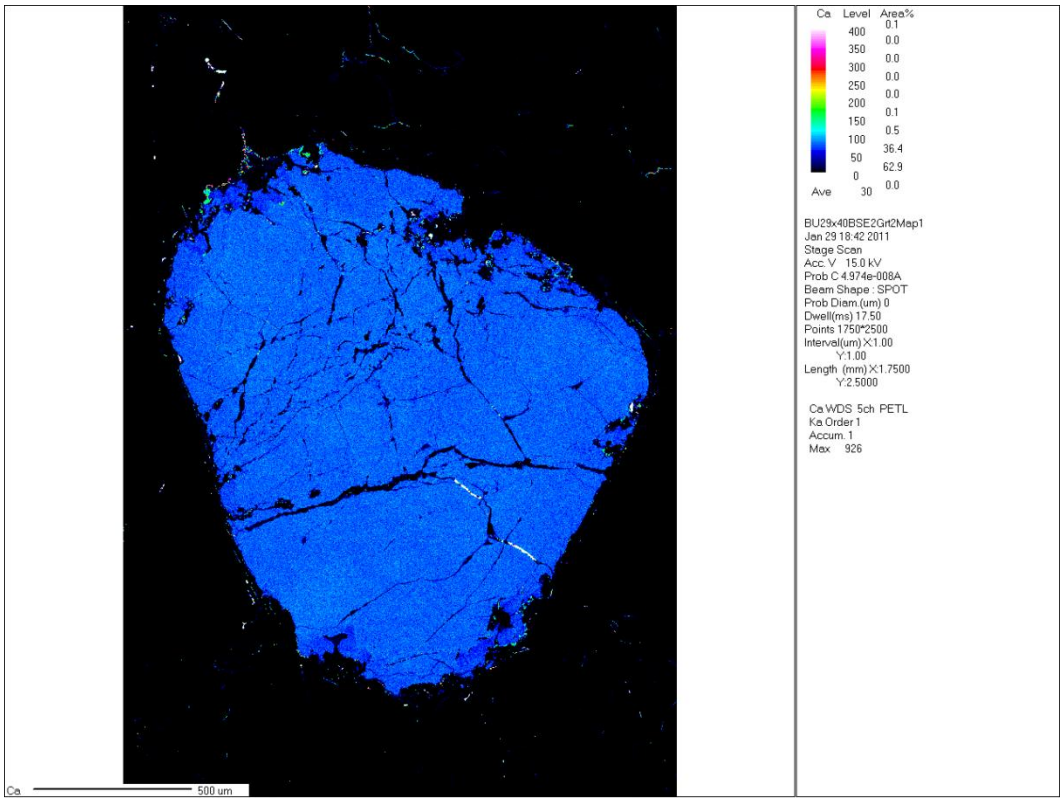

BU 29: Chromium

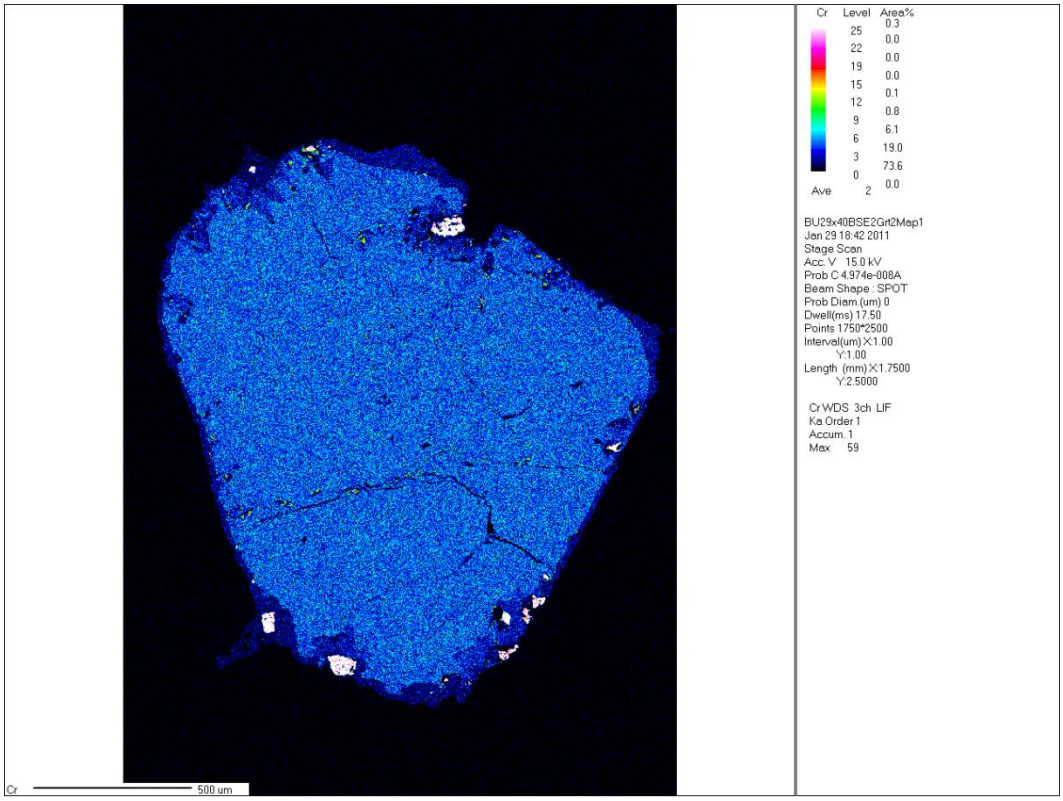

BU 29: Iron

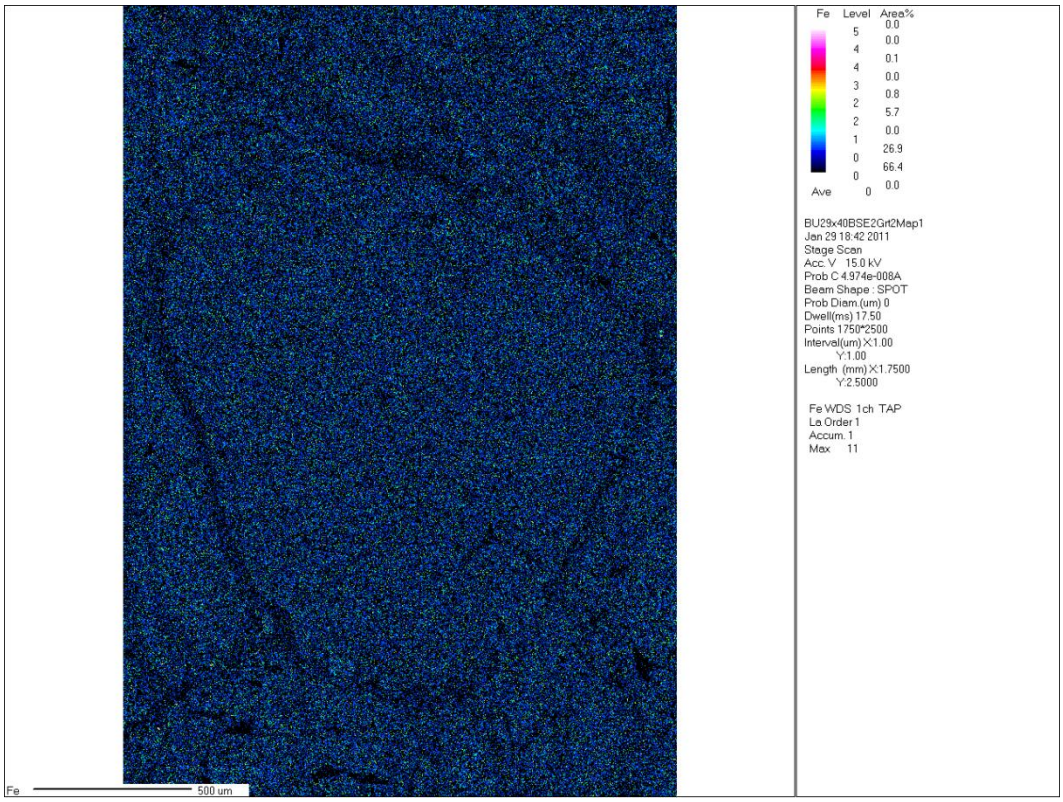

BU 29: Magnesium